Supporting Information for "On the relationship between excited state lifetime and isomerization quantum yield in animal rhodopsins: beyond the one-dimensional Landau-Zener model"

Mohsen M. T. El-Tahawy[‖,ᵃ] , ArturNenov[‖], Oliver Weingart[§], Massimo Olivucci[‡,⊥,*], Marco Garavelli[‖,*]

[‖]Dipartimento di Chimica Industriale "Toso Montanari", Università degli Studi di Bologna, Viale del Risorgimento, 4I -40136 Bologna, Italy.

[ᵃ]Chemistry Department, Faculty of Science, Damanhour University, Damanhour 22511, Egypt.

[§]Institut für Theoretische Chemie und Computerchemie, Heinrich-Heine-Universität Düsseldorf, Universitätsstr. 1, 40225 Düsseldorf, Germany.

[‡]Dipartimento di Biotecnologie, Chimica e Farmacia, Università di Siena, I-53100 Siena, Italy.

[⊥]Chemistry Department, Bowling Green State University, Bowling Green, OH 43403.

Table of Contents

1   Definitions

Here we report the definitions of terms mentioned in the main text.

Bond length alternation (BLA♣) defined as the difference between the average single-bond and the average double-bond; Quantum yield (QY): is defined as the ratio between the trajectories reaching bathoRh over the total number of trajectories; Lifetime τ: defined as the time period it takes for half of the population to decay to the GS; Decay window: defined as twice the standard deviation of hopping events times; The average electronic population: defined as the sum of squared coefficients of each state; The trajectory occupation: defined as the ratio of trajectories in each state; The time of transition of the GS wavefunction from CT to covalent: defined as the time when the total charge on the N-terminus (C_{12}—N segment) reaches +0.9 e; Decision events: defined as the time step at which the charge at the N-terminus has grown to +0.9 e, indicating a completed transition of the GS wavefunction from CT to covalent; the total charge on the N-terminus: defined as the sum of all Mulliken charges in the C_{12}...N segment.

2   Methodology and Benchmarking

2.1   Three Pigments Models

One of the prerequisites of our computational study is the construction of a computer model starting from the crystal structure of the three pigments. In contrast to both Rh and sqRh, there is no available crystallographic data for hMeOp. Therefore, Rinaldi et. al. have exploited the high sequence similarity between sqRh, whose crystal structure is available (PDB code: 2Z73) [1], and hMeOp (40%) to construct an atomistic structural model of hMeOp (**Figure S1**). Here we employ the same models used in the study of Rinaldi et al. for the three pigments [2]. Briefly, the QM/MM models of Rh and sqRh were prepared utilizing only one unit of the

---

♣ $BLA = \dfrac{C_6C_7 + C_8C_9 + C_{10}C_{11} + C_{12}C_{13} + C_{14}C_{15}}{5} - \dfrac{C_5C_6 + C_7C_8 + C_9C_{10} + C_{11}C_{12} + C_{13}C_{14} + C_{15}N}{6}$

dimeric crystallographic structures (chain A) in which all the crystallographic water molecules were included while the membrane lipids at the protein surface were excluded (for Rh: PDB code 1U19 [3], resolution 2.2 Å; for sqRh: PDB code 2Z73 [1], resolution 2.5 Å). On the other hand, the QM/MM model of hMeOp was constructed by homology modeling, i.e. starting from the crystallographic structure of sqRh as a template in which the retinal chromophore coordinates were kept fixed as in sqRh. This protocol of comparative modeling was validated by reproducing the observed absorption maximum for the human rhodopsin using the crystallographic structure of bovine Rh (95% sequence similarity) as a template [2].

2.2   QM/MM Partitioning Scheme

The QM/MM approach has been extensively used for modeling RPSBs in solution and in proteins[2, 4-8]. Our QM/MM models for the three rhodopsins are based on an high-medium-low QM/MM scheme in which the QM/MM boundary was placed on the Lys Cδ–Cε bond and the link−atom approach was used to model the frontier (**Figure S2**)[9-11]. The whole PRSB chromophore is treated quantum mechanically (54 atoms including the link atom) keeping the protein environments fixed at their crystal structure atomic positions except the closest 9 atoms of the lysine side−chain connected to the PRSB were free to move (i.e., as M layer). The protein environments were described by a modified AMBER96 force field. Electrostatic embedding was used to describe the interaction between MM and QM systems [6].

Figure S1. Comparative model (violet) of hMeOp superimposed on top of sqRh crystallographic structure used as template (green), this **Figure** taken from ref [2].
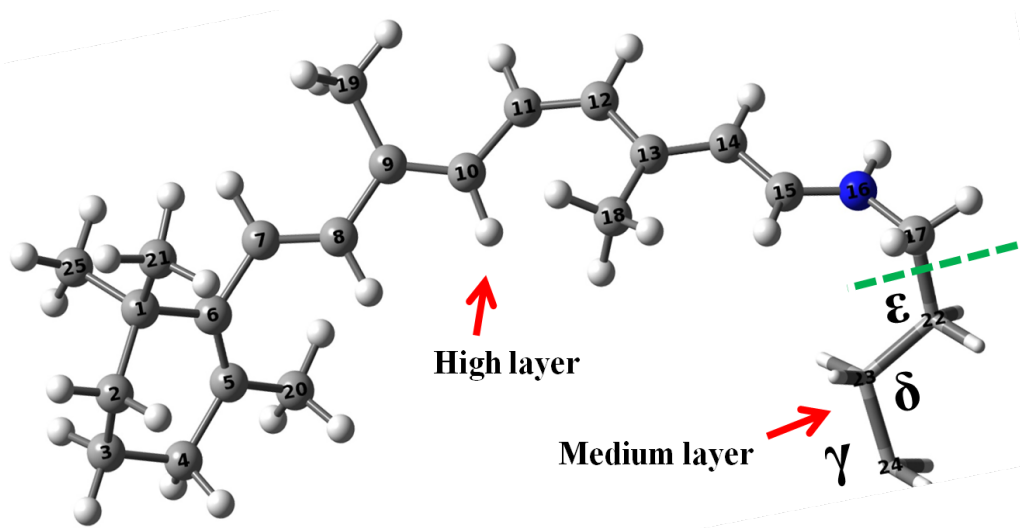
Figure S2. Schematic representation for high and medium layers, the green dashed line shows the cut between the H and M layers. The atoms in ball and stick representations belong to the QM region while atoms represented as tubes belong to the medium layer. The low layer includes the rest of the protein not shown in the figure.

2.3 Optimization and Single Point Calculations

The ground state structures of the three pigments were optimized at the complete active space self−consistent field CASSCF/6−31G*/AMBER level with single root employing CAS (10,10) and CAS(12,12) active spaces (see next section). The CASSCF calculation was followed by subsequent multiconfigurational second−order perturbation theory (CASPT2) computations to estimate the dynamic correlation energy of each state in order to get a more quantitative evaluation of the excitation energies as well as generate the linear absorption spectra and to estimate the relaxed scan along the CCCC coordinate[12]. This combined CASPT2//CASSCF approach has been shown to return experimentally accurate energies with errors within 0.2-0.3 eV[13-14]. An imaginary level−shift of 0.2 au was used to decrease the influence of weakly interacting intruder states in the CASPT2 calculations[15]. The ionization potential and electron affinity parameter was set to 0.0 au [16], in accordance with previous studies of retinal in gas−phase and its protein environment[13, 17-19].

4

2.4   Selecting the Active Space

The complete active space CAS(12,12) of RPSB comprises twelve electrons in twelve π–orbitals (**Figure S3**), yet such a large active space may be practically used for optimization but it is impractical for frequency calculations and extensive dynamics simulations. A possible way to overcome this problem is to reduce the active space to ten electrons in ten π–orbitals CAS(10,10) by rejecting one occupied and one virtual π–orbitals from the full π–system. In order to select the two orbitals that have the least pronounced effect on the results we have computed for each pigment a single adiabatic trajectory with zero initial velocity (i.e. 0K reference trajectory) employing both the full-π CAS(12,12) and the a reduced active space CAS(10,10). For this purpose, many trials have been performed, each time excluding a couple of π/π*–orbitals (i.e. one occupied and one virtual). Eventually, the reduced active space that most accurately reproduced the reference CAS(12,12) trajectories was selected for running systematic dynamical studies.

We found that the trajectories computed with a CAS(10,10 excluding the pair of bonding and non-bonding π-orbitals localized on the β-ionone ring (**Figure S3**) reproduced perfectly both the energy profiles and the structural features shown using the full-π CAS(12,12) active space along the whole photoisomerization path (**see Figure S4 and Figure S5**). The resulting orbital set was therefore used for dynamics computations.
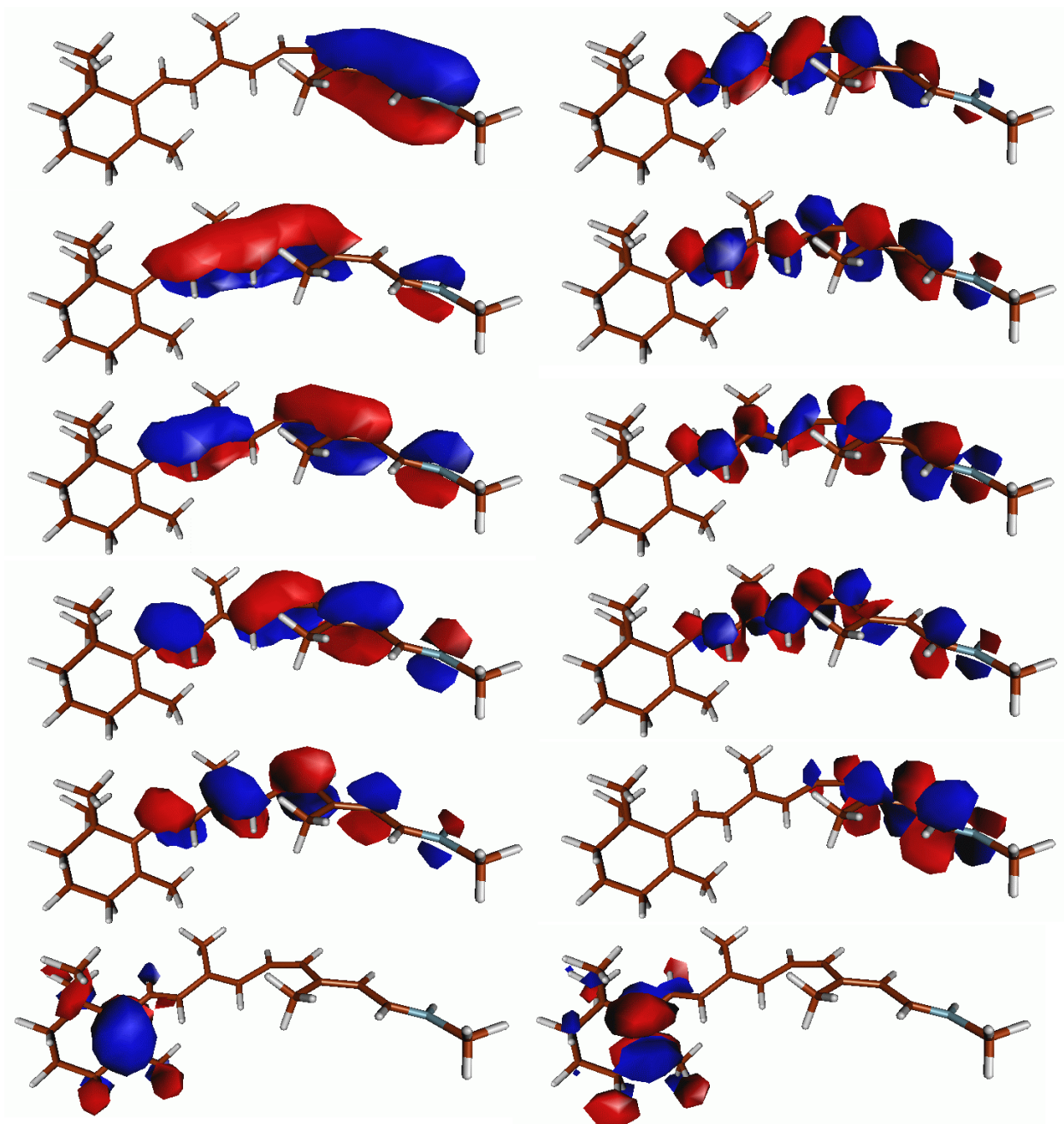
Figure S3. The molecular orbitals comprising the full active space CAS(12,12). Highlighted in gray is the neglected pair of bonding and anti-bonding orbitals resulting in the reduced CAS(10,10) which best reproduces the energy profiles and the structural features obtained using the full-π active space.

2.5 MD Simulations

2.5.1 0K Trajectories

Reference trajectories (FC trajectories) were started without any initial kinetic energy for the three pigments at at the CASSCF/6−31G*/AMBER96 level using two different active spaces CAS (10,10) and CAS (12,12) starting from the corresponding optimized FC

geometries. S_1 excited state trajectories were calculated at the same level of theory used for ground state optimization, but with state–averaging (weights: 0.5, 0.5) employing time steps of 0.5 employing both (10,10) and (12,12) active spaces. The time step was reduced to 0.25 fs in the vicinity of the crossing between S_0 and S_1 (i.e. ΔE_{S1-S0}<15 kcal/mol); surface hopping was suppressed, i.e. the molecules were forced to stay in the excited state during the whole simulation.

While the agreement between computed and experimental absorption band and λ_{max} values supports the qualitative reliability of the limited ensemble generated by the sampling procedure, one could ask if the CASSCF method, which does not account for a significant part of the dynamic electron correlation, can be used to perform semi-classical trajectory calculations correctly. This question is important when the missing dynamic electron correlation has different weights in the S_1 and S_2 states. In other words, S_2 and S_1 would be well separated and thus the ES progression would be completely driven by the S_1 potential energy surface, after dynamic electron correlation energy correction (i.e. after re-computing the energy profiles at the SS-CASPT2 or MS-CASPT2 levels) while at the CASSCF level the S_2 state may mix with S_1 and seriously interfere with the S_1 motion.

In order to provide evidence that this potential issue is not significantly affect the presented results, we have computed and analyzed three QM/MM semi-classical trajectories (also called FC trajectories) which were calculated by starting at the corresponding FC points on the S_1 energy surface without initial velocities and propagating until reaching the S_1/S_0 intersection seam (the same trajectories were presented in ref.[2]). In principle, such trajectories follow the minimum energy path along the ES potential energy surface and are assumed to provide information on the dynamics of the center of the excited state population (i.e. the vibrational wavepacket) projected on the ES upon excitation[20]. The analysis of the Rh, sqRh and hMeOp FC trajectories shows that the S_2/S_1 mixing is noticeable only in the FC region and last just few fs. In other words, within 10 fs the electronic structure of the S_1 state acquires a pure charge transfer character in all systems consistently with previous works on Rh[2, 21], **Figures S4 and S5.**

We conclude that the only change resulting from the SS-CASPT2 or MS-CASPT2 corrections is a decrease in the slope of the S_1 potential energy surface connecting the FC point to the CI. As elaborated previously such change translates in a proportionality in the resulting energy gradients and, finally, in a scaling factor to the simulation time[2, 21] but it should not

affect the qualitative outcome of the comparison. On this basis, we assume that the trends in ES lifetimes and QYs will not change when using the CASSCF force field.
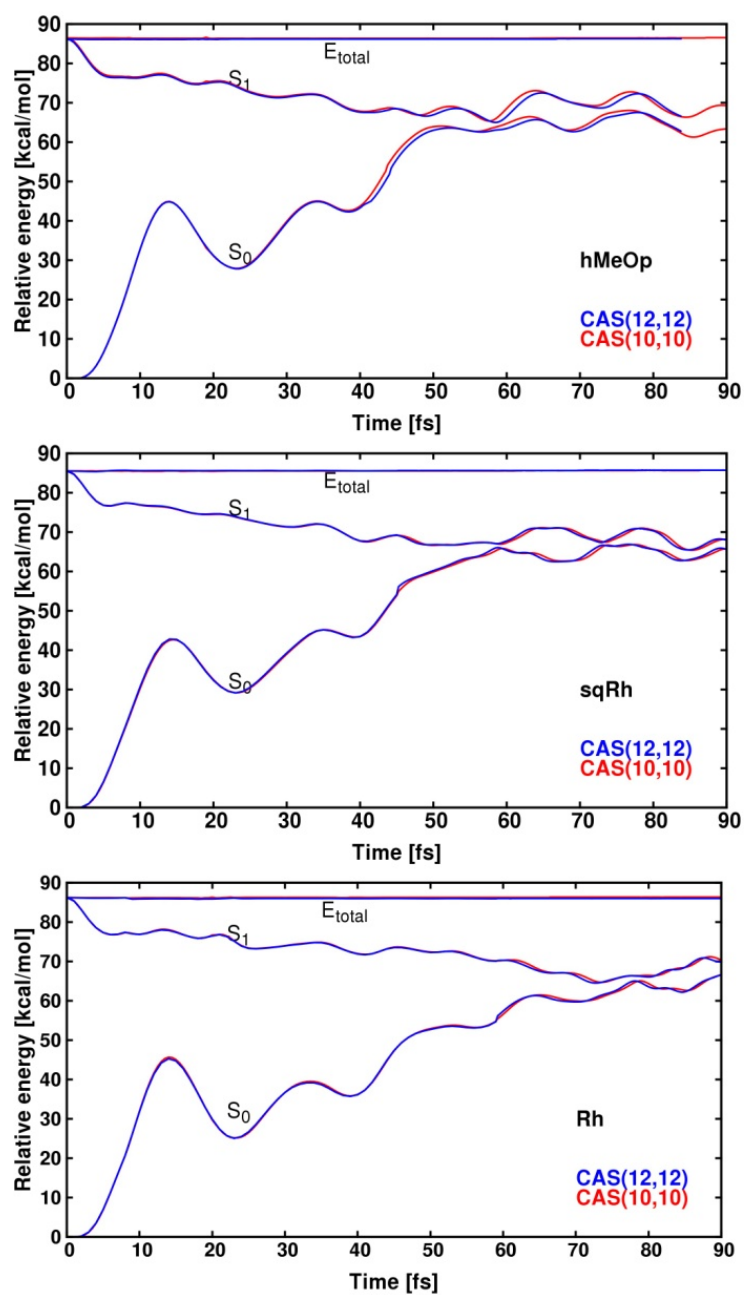
Figure S4. Overlay of S_1 and S_0 and total energies in pigment trajectories computed with CAS (10,10) and CAS (12,12) active spaces shown in red and blue colours, respectively. The CAS space has virtually no influence on the excited state dynamics.
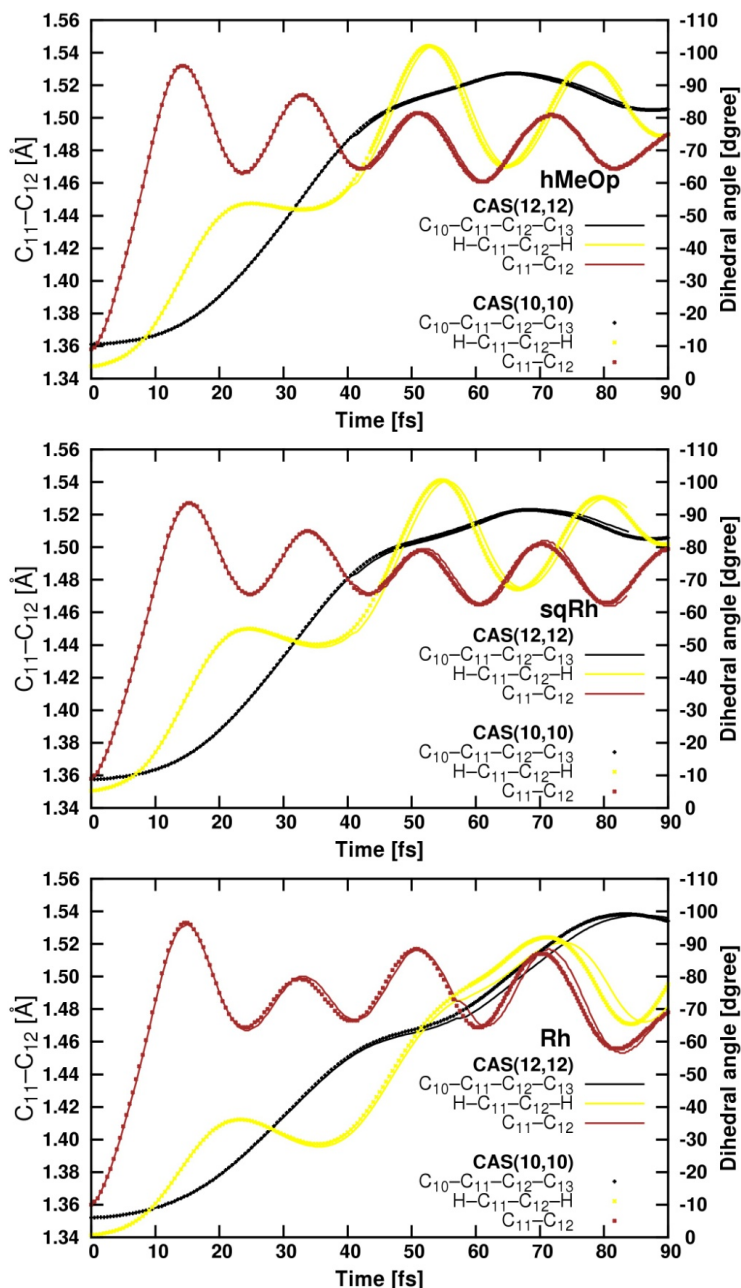
Figure S5. Overlays of $C_{11}-C_{12}$ bond length, $C_{10}-C_{11}-C_{12}-C_{13}$ and $H-C_{11}-C_{12}-H$ dihedrals in 0K trajectories computed with CAS(10,10) (dashed lines) and CAS(12,12) (solid lines) active spaces.

2.5.2   Trajectory Swarms

On the basis of the demonstrated similarity of the results of the 0K trajectories produced with the two active spaces, CAS (10,10) was employed for the computation of the room temperature trajectory swarms. For each pigment, numerical frequencies were calculated on top of the re−optimized ground state CASSCF(10,10)/6−31G* geometries. A set of 60 geometries with their associated velocities were created using thermal sampling option as implemented in Gaussian 03[22] at a temperature of 300K. This routine considers the zero-point energy and additional temperature effects by exciting the vibrational modes according to Boltzmann statistics. Such set of initial conditions is intended to mimic the wave packet nature

of the quantum-mechanical system. The molecular dynamics simulations were started in the bright excited state (S_1) employing a two root state averaged CAS(10,10)/6-31G* description and a time step of 0.5 fs. The time step was reduced to 0.25 fs in the vicinity of a crossing (i.e. ΔE_{S1-S0}<15 kcal/mol). Trajectories were propagated with a velocity Verlet algorithm at constant total energy[23]. The surface hop between S_1 and S_0 potential energy surfaces was activated: a Tully's fewest switches surface hopping algorithm with decoherence correction (d = 0.1 au) [24] was used for this purpose. Back hopping to the ground state was suppressed during simulation. Trajectories were computed up to the formation of clear ground state photoproducts through tracking the evolution of the C_{10}–C_{11}–C_{12}–C_{13} torsion angle. The molecular orbitals calculated using MOLCAS 7 [23] were transformed to MOLPRO 2009 [9, 25] in order to calculate the non-adiabtic coupling vectors. All QM/MM single point, geometry optimizations, numerical frequency and molecular dynamic calculations have been performed using COBRAMM, a QM/MM program interfacing various QM and MM codes [8, 25-27].

2.6   Time Scaling of the Excited–State Trajectory

It is well established that the missing dynamical correlation at the CASSCF level may affect significantly the energy profiles and thus the resulting non-adiabatic dynamics. This may result in erroneous state ordering, different potential energy surface topography, variations in activation barriers, topology of conical intersections, etc. In ref. [21] Olivucci and co-workers showed that under the assumption of a linear relation between the CASSCF and CASPT2 energies, CASPT2 corrected time scales and energy profiles can be obtained. This assumes that that the energies are related via a proportional factor α according to the relation:

$$\alpha E_{CASSCF}(x) = E_{CASPT2}(x) \ (1)$$

The factor **α** in the energies translates into a proportionality in the resulting energy gradients. Furthermore, the authors showed that the linear relation holds for Rh by exploring the minimum energy path at CASSCF and CASPT2 levels. They demonstrated that the uncorrelated CASSCF energy profile is steeper than the correlated CASPT2 profile, resulting in α values < 1.0, and, hence, smaller gradients. Furthermore, they argued that since the molecular dynamics explores a region of the PES that is close to the reaction path, one may assume that this relation is also valid along any computed trajectory. As the gradient enters in the Velocity-Verlet algorithm as the system's acceleration during the molecular dynamics its scaling has an immediate effect on the simulation's time:

$$t_{scaled} = t_{unscaled}\alpha^{\frac{1}{2}} \ (2)$$

where $t_{unscaled}$ is the "unphysical" time resulting from the CASSCF dynamics, and t_{scaled} is the scaled "physical" time that would be obtained if the dynamics would have been run at the CASPT2 level. Assuming that the same linear relation α, holds also in the pigments investigated in this study we have calculated the CASPT2 and CASSCF excited–state energies along the reaction path from the relaxed FC region to the conical intersection with the ground state by means of a relaxed scan around C_{10}-C_{11}-C_{12}-C_{13} torsional coordinate with 10° increment. The values for the parameter α were then obtained by linear fitting of the corresponding energies of S_0, S_1 and ΔE (**Figure S6, S7 and Table S1**). The linear relation for all three pigments holds well in the explored region (R^2 value of 0.99) giving an averaged scaling factor α~0.81 for all three pigments being consistent with the previously reported Rh value (0.795) based on fitting the energy of the S_1 state [21].
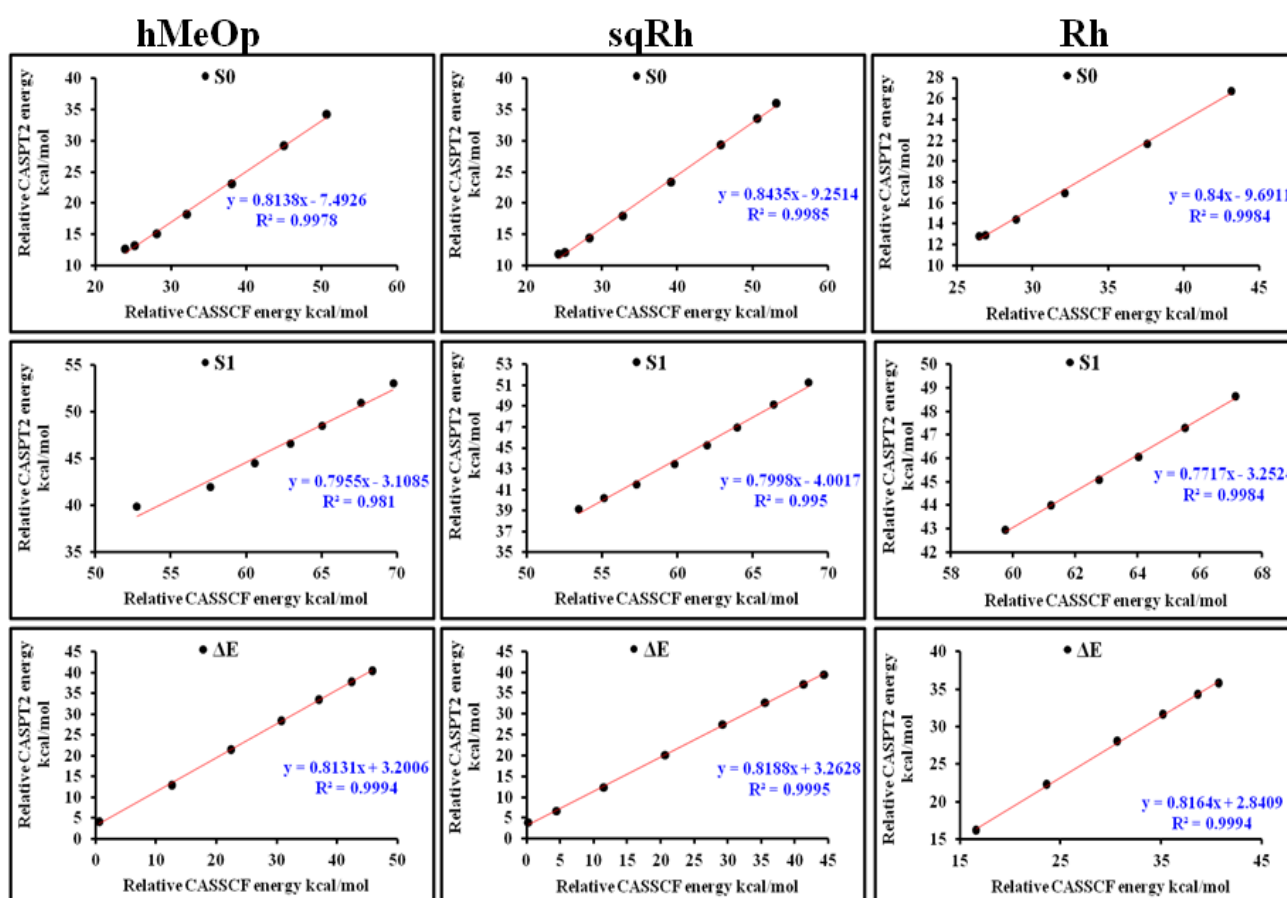
Figure S6. Linear fit of relative energies (referred to the ground–state minimum) calculated at CASPT2 and CASSCF level of theory along the computed CASSCF reaction path.

Table S1. α values according the linear fitting between CASSCF and CASPT2 of S_0, S_1 and ΔE energies

	S_0	S_1	ΔE	Average
hMeOp	0.8138	0.7955	0.8131	0.811
sqRh	0.8435	0.7998	0.8188	0.832
Rh	0.8400	0.7717	0.8164	0.798
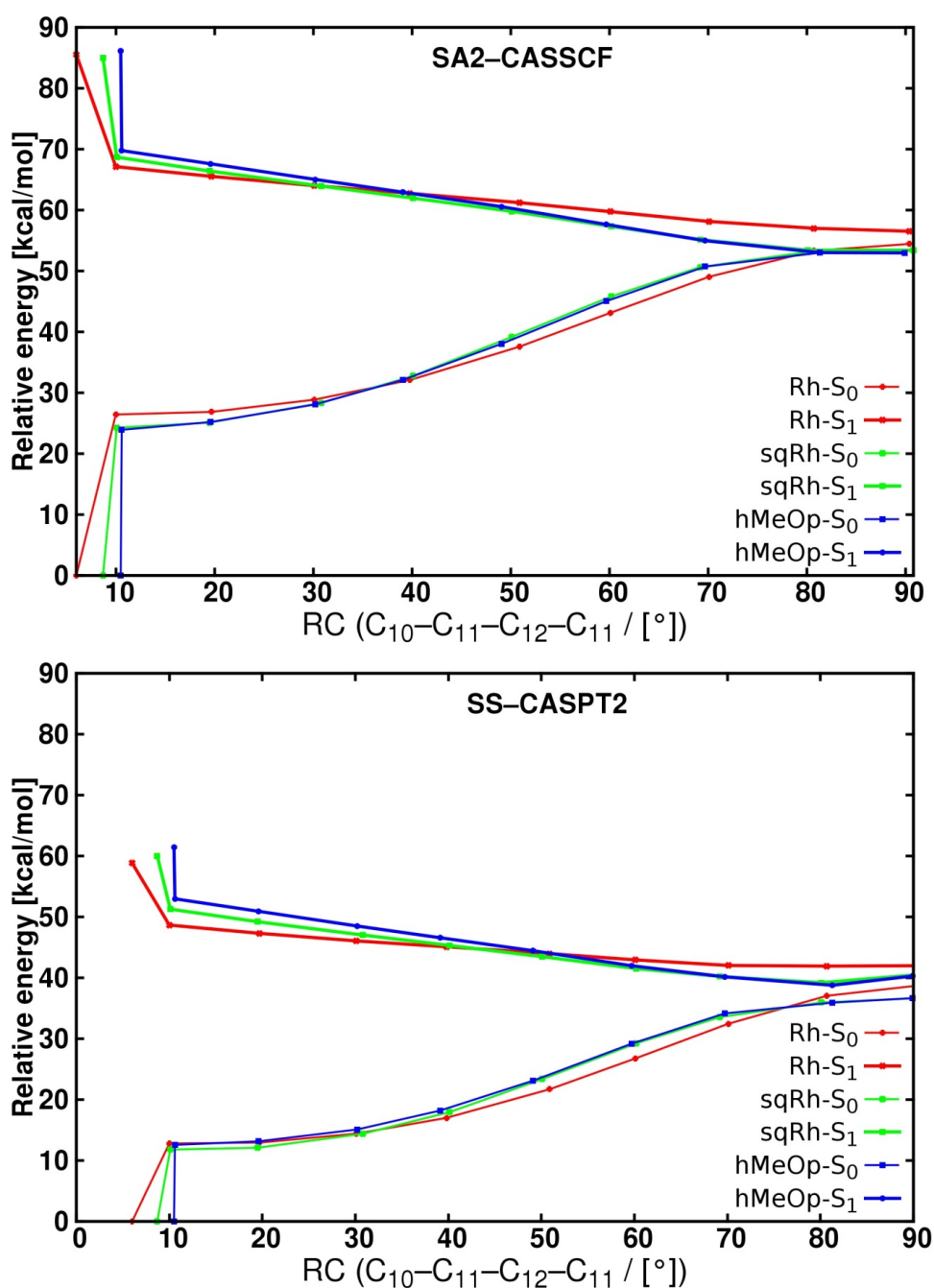
Figure S7. SA2–CASSCF(12,12)6–31G*/AMBER and SS-CASPT2 energy profiles along the torsion angle C_{10}–C_{11}–C_{12}–C_{13} obtained from constrained relaxed scan with 10° increment.

3 Geometrical and Electronic Structures of the models

The constructed QM/MM models reproduce the results of Rinaldi et al.[2] and is here briefly summarized. The S_0 equilibrium structures show a similar BLA positive value of ca. 0.12 Å corresponding to a clear alternating single-double bond pattern with limited delocalization. The cavity embedding distorts the conjugated chain out-of-plane with respect to the gas-phase equilibrium structure of rPSB11. In fact, we observe a progressive increase of the CCCC dihedral in the series Rh (-6°)→sqRh (-9°)→hMeOp (-11°), as well as a notable -17° (Rh), -23° (sqRh) and -19° (hMeOp) deviation from planarity of the C_{11}-C_{12}–C_{13}-C_{14} dihedral describing the twisting about the single bond adjacent to the reactive C_{11}-C_{12} double bond. In contrast, the β–ionone ring exhibits a less pronounced twisting with respect to the gas-phase rPSB11 equilibrium structure (-66°), with hMeOp and sqRh displaying values of ca. -60° and Rh displaying a value of ca. -55° (Table S2).

In all cases, the S_0→S_1 vertical excitation corresponds to a bright state (i.e. it features a large oscillator strength) with a dominant contribution of the HOMO→LUMO (see Figure S3) transition resulting in a S_1 state with charge transfer character with respect to the S_0 which is covalent. By covalent character we refer to the usual covalent bonding where the electrons forming the π-component of the –C_{11}-C_{12}– double bond reside on C_{11} and C_{12} and are single spin coupled. This differs from the charge transfer character of –C_{11}(+)–C_{12}= type[28]. In contrast, S_0→S_2 is dominated by the HOMO→LUMO double excitation and HOMO-1→LUMO single excitation and has limited oscillator strength consistent with a dominant open-shell diradical character. The computed vertical excitation energies reproduce, when converted in wavelength values, the trend of observed absorption maxima (λ_{max}) with Rh featuring a red-shifted λ_{max} with respect to sqRh and hMeOp which have 1 and 2 kcal/mol larger excitation energies (Table S3), respectively (notice that, all computed excitation energies are, systematically blue-shifted by ca. 2 kcal/mol[2] with respect to the experimental quantities[29-31]).

As established for rhodopsins[32-34], λ_{max} values are determined by the non-uniform electric field generated by the protein cavity. In the studied pigments the electrostatic interaction introduces a strong blue-shifting effect of ca. 8 kcal/mol for hMeOp and sqRh and 7 kcal/mol for Rh (SS-CASPT2 level). In hMeOp and in sqRh the effect is dominated by E215 and E172 which change the excitation energy by ca. 5 and 9 kcal/mol, respectively, when set to zero. These E215 and E172 residues are homologous to the E181 secondary counterion of Rh, which

has only a small effect on the Rh excitation energy. In fact, the excitation energy in Rh is dominated (ca. 18 kcal/mol blue-shifting effect) by the interaction with the E113 primary counterion[2].

The conformational distortion of rPSB11 induced by the different protein cavities also influences the λ_{max}. In fact, the excitation energy trend displayed by the three rhodopsins is retained in the corresponding chromophores when these are extracted from their protein cavities (or equivalently, when all protein charges are set to zero). This behavior, can be correlated to the progressive increase of the CCCC value (see above).

Table S2. The ground state geometrical parameters optimized using CAS(12,12) and CAS(10,10) active spaces

Parameter | Moodel	CAS(12,12)				CAS(10,10)		
	Rh	**sqRh**	**hMeOp**	**Vac.**	**Rh**	**sqRh**	**hMeOp**
C_5-C_6	1.352	1.351	1.354	1.353	1.332	1.332	1.334
C_6-C_7	1.493	1.491	1.494	1.493	1.494	1.491	1.495
C_7-C_8	1.352	1.346	1.348	1.349	1.351	1.347	1.348
C_8-C_9	1.474	1.469	1.471	1.471	1.474	1.470	1.472
C_9-C_{10}	1.361	1.359	1.360	1.364	1.361	1.359	1.360
$C_{10}-C_{11}$	1.464	1.459	1.459	1.451	1.465	1.459	1.459
$C_{11}-C_{12}$	1.360	1.358	1.357	1.363	1.360	1.358	1.357
$C_{12}-C_{13}$	1.466	1.471	1.467	1.460	1.466	1.471	1.467
$C_{13}-C_{14}$	1.370	1.364	1.365	1.370	1.370	1.364	1.365
$C_{14}-C_{15}$	1.434	1.425	1.429	1.428	1.435	1.425	1.429
$C_{15}-N_{16}$	1.292	1.294	1.293	1.292	1.292	1.294	1.293
$C_5-C_6-C_7-C_8$	−54.9	−61.6	−60.7	−65.7	−55.4	−62.8	−61.9
$C_6-C_7-C_8-C_9$	179.3	−177.6−	178.7	−178.6	179.3	−177.4	178.8
$C_7-C_8-C_9-C_{10}$	−173.5	176.0	171.2	179.5	−172.4	176.3	171.2
$C_8-C_9-C_{10}-C_{11}$	173.9	177.9	178.0	179.9	173.8	178.0	178.0
$C_9-C_{10}-_{C11}-C_{12}$	163.1	165.1	164.6	176.4	163.3	165.0	164.5
$C_{10}-C_{11}-C_{12}-C_{13}$	−6.0	−8.8	−10.6	−2.7	−6.0	−8.7	−10.5
$C_{11}-C_{12}-C_{13}-C_{14}$	163.0	156.6	161.0	175.7	163.1	156.5	160.9
$C_{12}-C_{13}-C_{14}-C_{15}$	−178.3	179.0	172.8	−179.8	−178.3	179.1	172.8
$C_{13}-C_{14}-C_{15}-N$	168.4	168.0	169.1	179.1	168.4	167.8	169.2
$H-C_{11}-C_{12}-H$	−0.7	−5.3	−3.8	−1.1	−0.7	−5.3	−3.8
$C_8-C_9-C_{10}-H$	−1.9	0.4	0.6	0.1	−1.9	0.5	0.6
$C_{14}-C_{15}-N-H$	−1.0	−0.3	−3.7	0.0	−0.9	−0.4	−3.7
$C_7-C_9-C_{10}-H$	177.2	179.1	−179.6	179.8	177.3	179.1	−179.6
BLA	0.12	0.12	0.12	0.11	0.12	0.12	0.12

Table S3. SS−CASPT2 and MS−CASPT2//CASSCF(12,12) and(10,10)/6−31G*/AMBER computed absorption maxima (λ_{max}, nm) and corresponding oscillator strengths f,

state–averaged over three roots (weights: 1/3, 1/3, 1/3) and calculated on top of the corresponding S_0 minima.

	Model	CAS (12,12)								CAS (10,10)								exp.
		SS-PT2				MS-PT2				SS-PT2				MS-PT2				
		$\lambda 1$	$\lambda 2$	f1	f2	$\lambda 1$	$\lambda 2$	f1	f2	$\lambda 1$	$\lambda 2$	f1	f2	$\lambda 1$	$\lambda 2$	f1	f2	$\lambda 1$
protein	hMeOp	468	326	0.64	0.3	452	313	1.2	0.1	463	325	0.7	0.3	449	312	1.2	0.1	467–480
	SqRh	477	329	0.58	0.3	463	316	1.1	0.1	469	328	0.6	0.3	458	314	1.1	0.1	489
	Rh	486	332	0.59	0.3	469	313	1.3	0.1	475	329	0.6	0.3	462	310	1.3	0.1	498
isolated	hMeOp	538	340	0.65	0.3	505	331	1.2	0.2	526	337	0.7	0.3	497	328	1.2	0.2	
	SqRh	545	344	0.62	0.3	513	335	1.1	0.3	531	339	0.6	0.3	502	330	1.1	0.2	
	Rh	554	349	0.67	0.3	518	340	1.2	0.3	530	339	0.7	0.3	499	330	1.3	0.2	
	Vac.	535	347	0.82	0.2	495	334	1.5	0.2									
	Vac.(-55)	549	350	0.8	0.2	504	337	1.5	0.2									

4   Absorption Band

Figure 8 depicts the experimental (dashed lines) and simulated (solid lines) linear absorption (LA) spectra of hMeOp, sqRh and Rh. The theoretical spectra were computed using the 60 snapshots of the three RT ensembles. These points are the same employed for starting the semi-classical trajectories. The spectra consist of an intense broad unstructured band in the Visible (Vis) with a maximum between 475 nm and 500 nm, hMeOp showing the most blue-shifted band, Rh the most red-shifted. Wavefunction analysis shows that the Vis band is associated with the $S_0 \rightarrow S_1$ transition. The $S_0 \rightarrow S_2$ transition is the source of a weaker band in the near-ultraviolet around 340 nm (not shown). We observe a nearly quantitative agreement between theory and experiment for Rh and a fair agreement in the case of SqRh, where the experimental spectrum shows a somewhat steeper decrease in the red. Interestingly, compared with the SS-CASPT2 level (Figure S8 bottom-panel), MS-CASPT2 better reproduces the experimental lineshapes (Figure S8 top-panel). The simulated spectrum of hMeOp strikes as the outlier in this comparison, showing a clear undersampling in the blue and, hence, reproducing only partially the blue-shift of the absorption band with respect to SqRh. There are two possible reasons for the discrepancy: a) due to the lack of a crystal structure hMeOp simulations rely on a homology model based precisely on SqRh, hence, disagreement with the experiment could be traced back to deficiencies of the model; b) hMeOp features the closest lying (and, hence, most strongly mixing) S_1 and S_2 states. As a consequence, MS-CASPT2 causes the largest energy splitting, thereby pushing the S_1 state too much to the red. Overall, the trend of the λ_{max} values in the spectra is consistent with the trend of the vertical excitation energies computed at the FC point (the former being 2-3 kcal/mol red-shifted as expected when the absorption energy is averaged over an ensemble of geometry realizations, see Tables S3 and S4).

While the agreement between computed and experimental λ_{max} values supports the qualitative reliability of the limited ensemble generated via the sampling procedure, it could be questioned if an inferior method like CASSCF, which is used to perform the molecular dynamics simulations, suffices to describe the pigment-specific characteristics of the electronic structure of the embedded RPSB.

In favor of the use of CASSCF we note that the ionic/covalent wavefunction mixing addressed above which requires a dynamically correlated treatment (MS-CASPT2 level) is particularly strong only in the FC region. Following its immediate departure (within 10 fs as elucidated below) the wavefunction of the S_1 state collapses to a pure CT, so that SS-CASPT2 and MS-CASPT2 give similar results. Furthermore, Figure S6 and Table S1 demonstrate that there exist a linear relation between the CASSCF and SS-CASPT2 potential energy surface profiles (at least along the minimum energy path) in all three systems, in line with previous works on Rh[2, 21]. As elaborated previously, the proportionality in the energies translates in proportionality in the resulting energy gradients and, finally, in a scaling factor to the simulation time[2, 21] but it should not affect the qualitative outcome of the comparison. Moreover, as foreshadowed in the previous section and elaborated below, the remarkable differences in the photoreactivity of the three pigments are to be also traced back to the mechanical tension in the catalytic cavity, which CASSCF is able to reproduce.

Table S4. SS−CASPT2 and MS−CASPT2//CASSCF(12,12)/6−31G*/AMBER calculation of averaged absorption maxima (λ_{max}, nm), vertical excitation energies ΔE (kcal/mol), oscillator strengths f, state−averaged using three roots (weights: 1/3, 1/3, 1/3) over all the 60 starting geometries of each pigment ensemble.

Model	SS−CASPT2						MS−CASPT2					
	λ_1	λ_2	ΔE_1	ΔE_2	f_1	f_2	λ_1	λ_2	ΔE_1	ΔE_2	f_1	f_2
hMeOp	496	351	57.8	81.9	0.59	0.24	478	331	60.0	86.8	1.14	0.10
SqRh	488	354	58.9	81.7	0.49	0.31	481	328	59.8	87.6	1.04	0.13
Rh	497	355	57.9	81.6	0.48	0.34	488	321	59.0	89.5	1.17	0.12
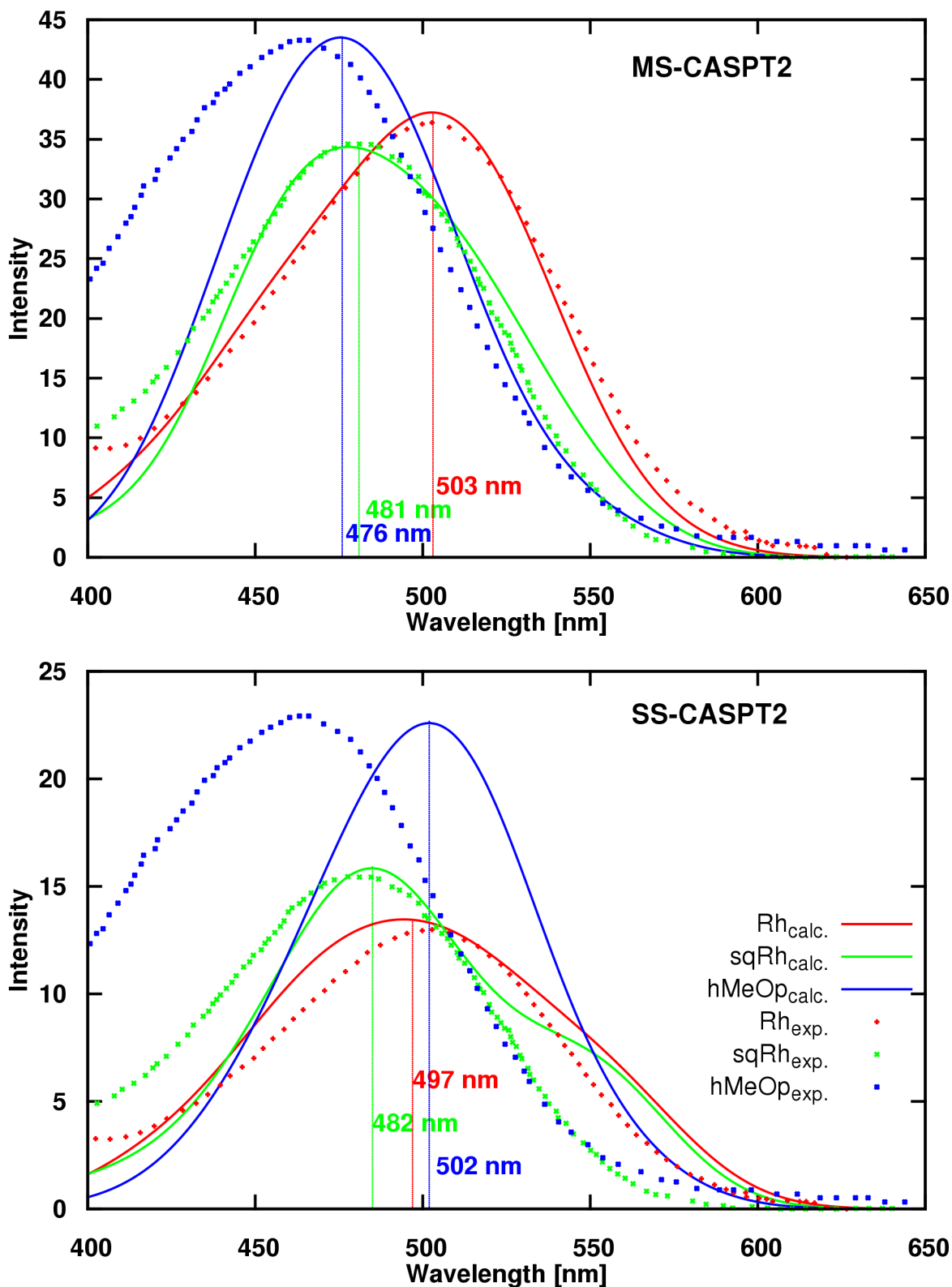
Figure S8. Experimental (dashed lines) and simulated (solid lines) linear absorption spectra of the three rhodopsins. Simulated spectra obtained from averaging over 60 realizations per pigment and corrected using MS-CASPT2 (top-panel) and SS–CASPT2 (bottom-panel) after SA3–CASSCF (12,12) calculations. Convolution based on wavelength values and S_1/S_2 oscillator strengths, Gaussian FWHM=53 nm. Exp. data taken from refs [29], [30] and [35] for hMeOp, sqRh and Rh, respectively.

17

5   Relationship between Vertical Excitation Energy, Steric Strain and Isomerization Speed
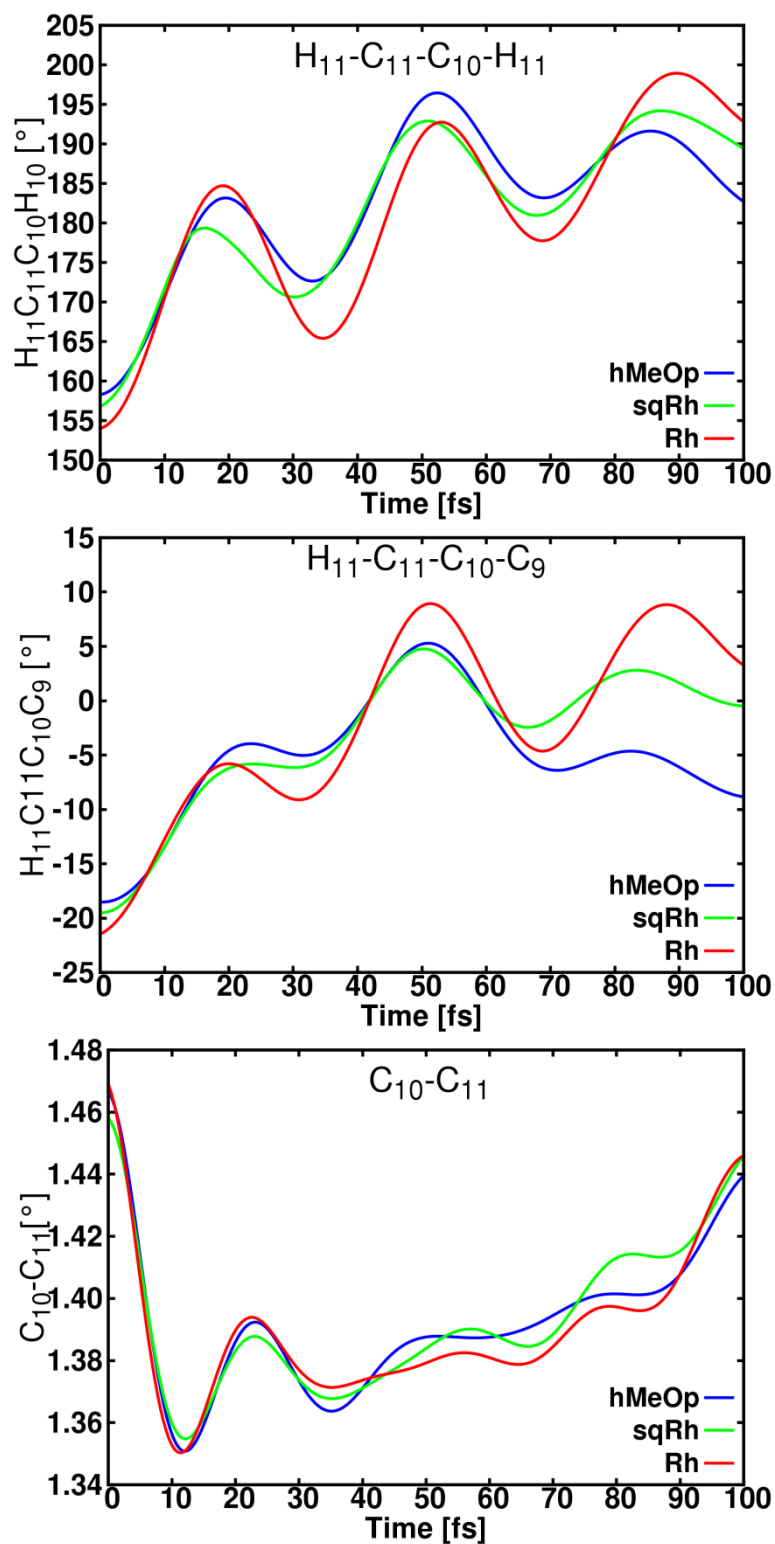
Figure S9. Characteristic geometrical parameters in the three pigments and their temporal evolution.

6 Rationalization of the Computed Quantum Yields
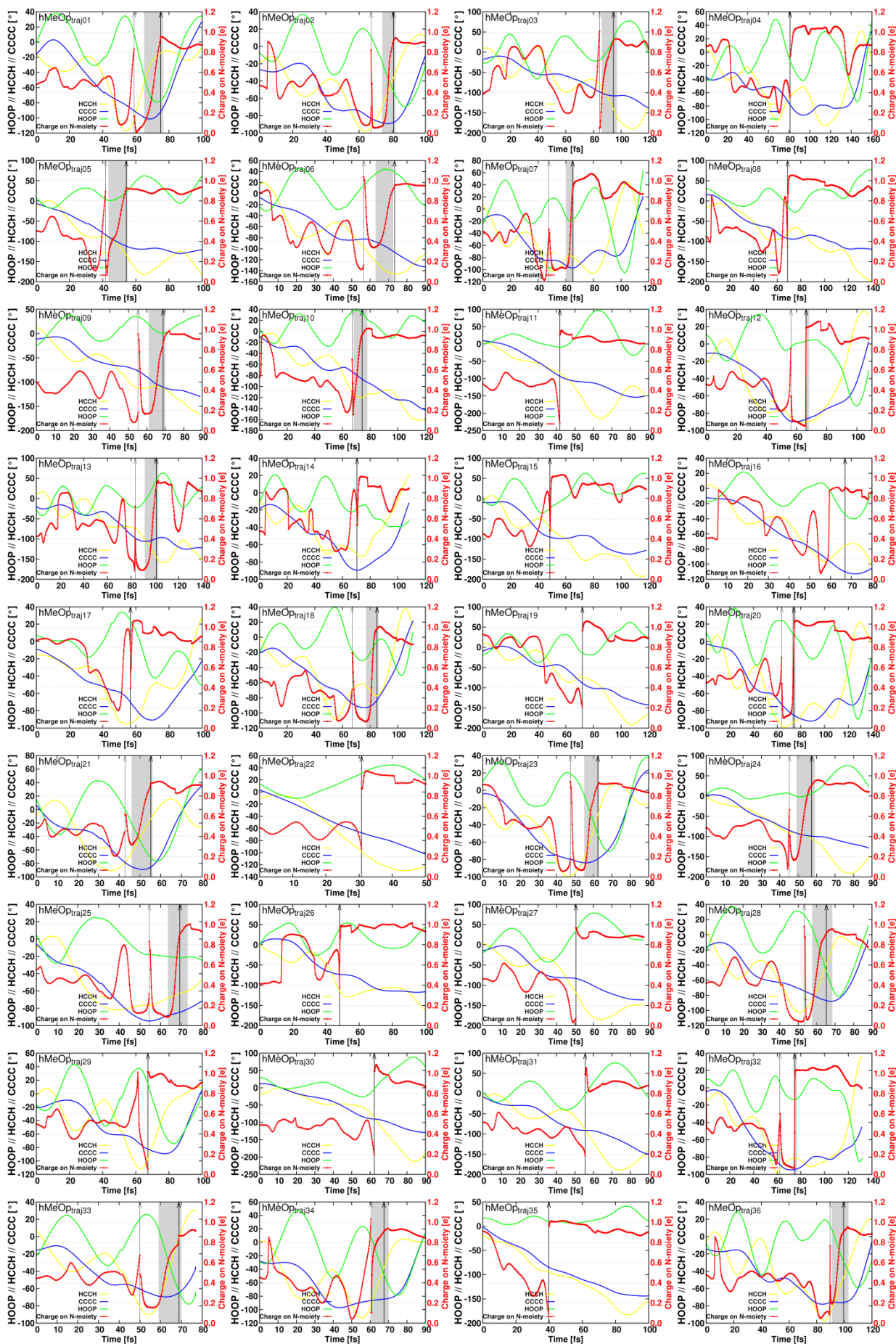
continue Figure S10
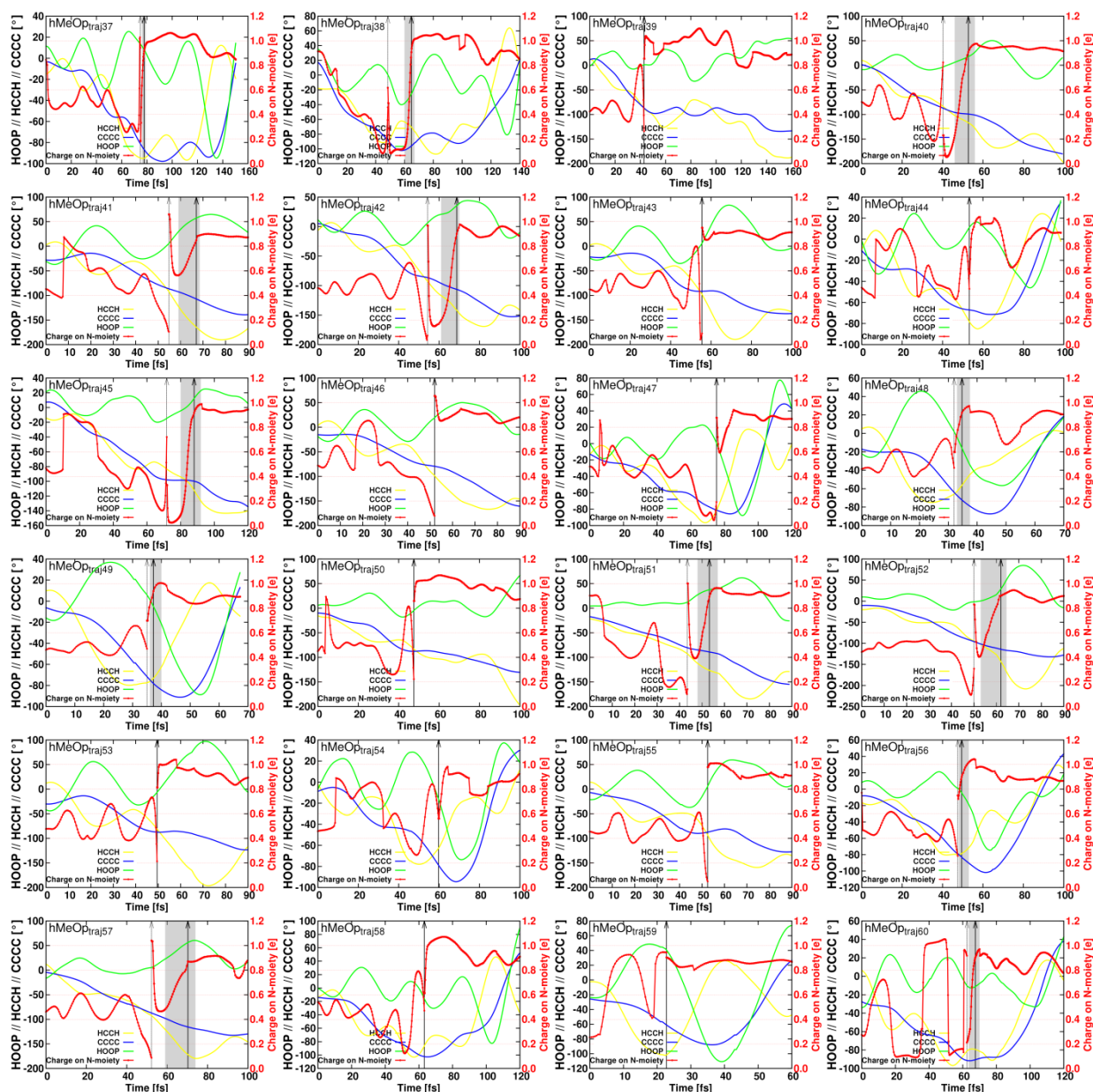
Figure S10. Evolution of $C_{10}C_{11}C_{12}C_{13}$, $H_{11}C_{11}C_{12}H_{12}$, HOOP ($C_{10}C_{11}C_{12}C_{13}$ - $H_{11}C_{11}C_{12}H_{12}$) and charge on N-moiety(C_{12}---N fragment) of each trajectory of hMeOp during the simulation time, gray-shaded areas denote the time span in which the WF changes from CT to covalent after a hopping event, vertical dashed and solid arrows show the hopping and decision times, respectively.

20
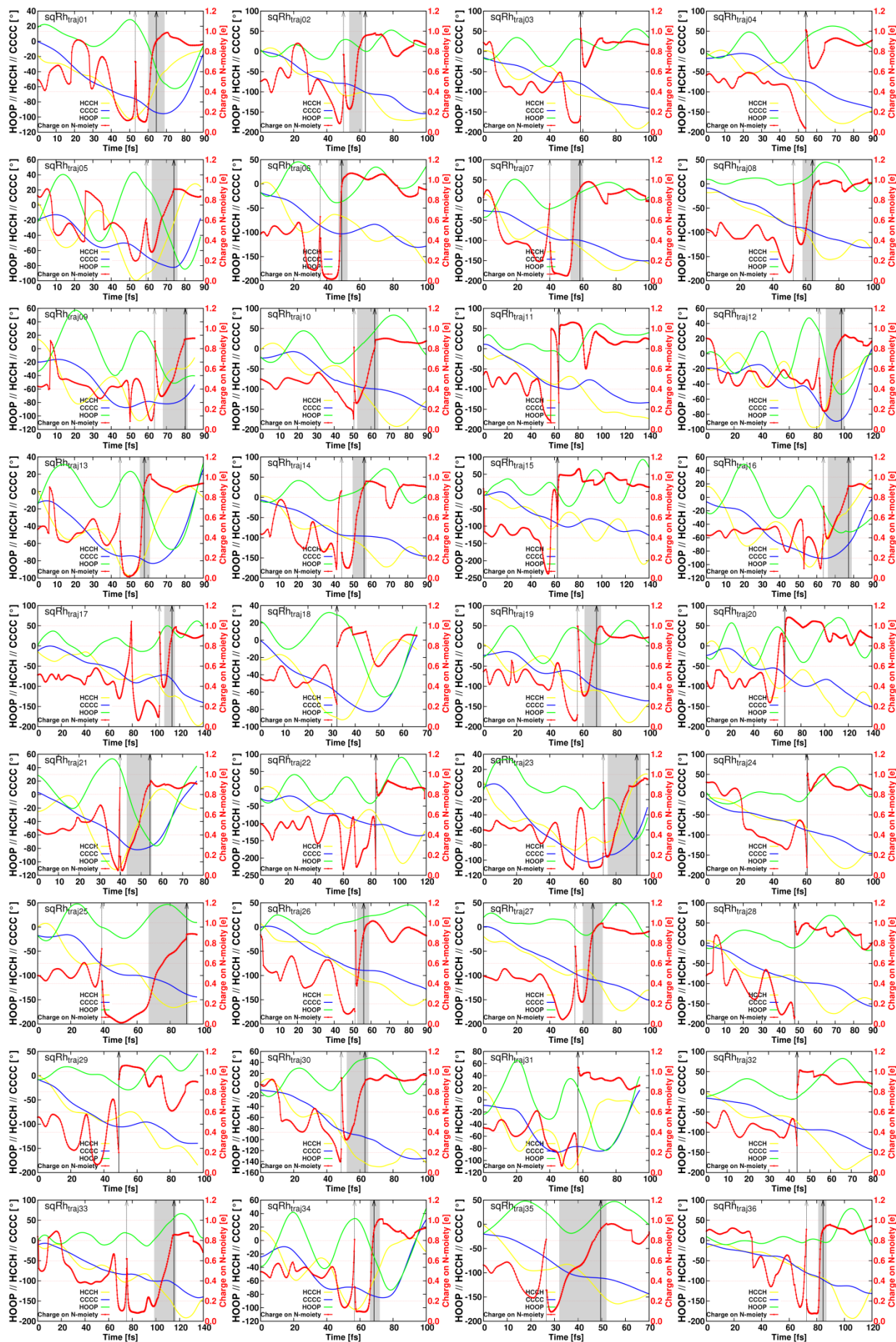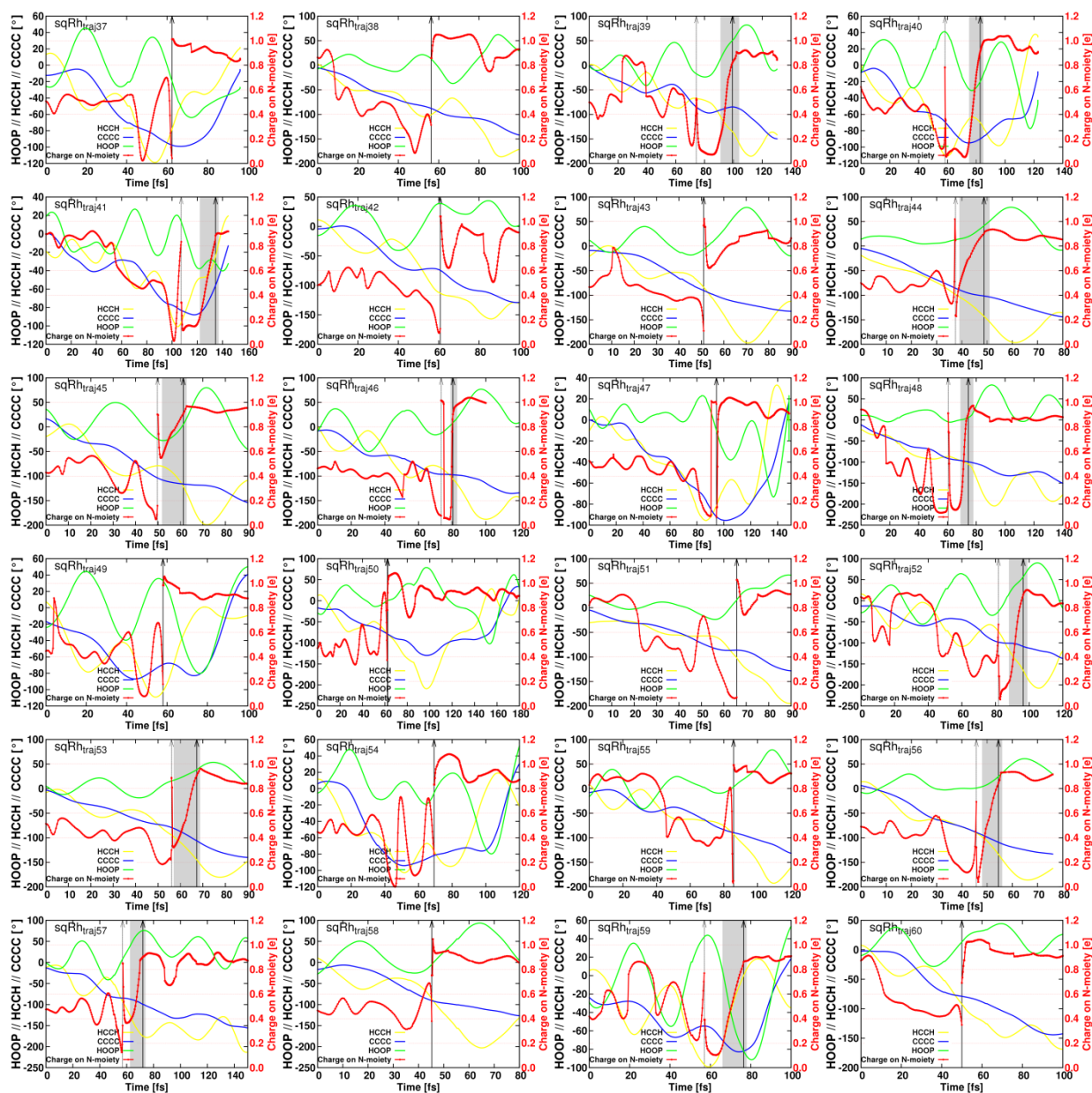
Figure S11. Evolution of $C_{10}C_{11}C_{12}C_{13}$, $H_{11}C_{11}C_{12}H_{12}$, HOOP and charge on N-moiety of each trajectory of sqRh during the simulation time, gray-shaded areas denote the time span in which the WF changes from CT to covalent after a hopping event, vertical dashed and solid arrows show the hopping and decision times, respectively.
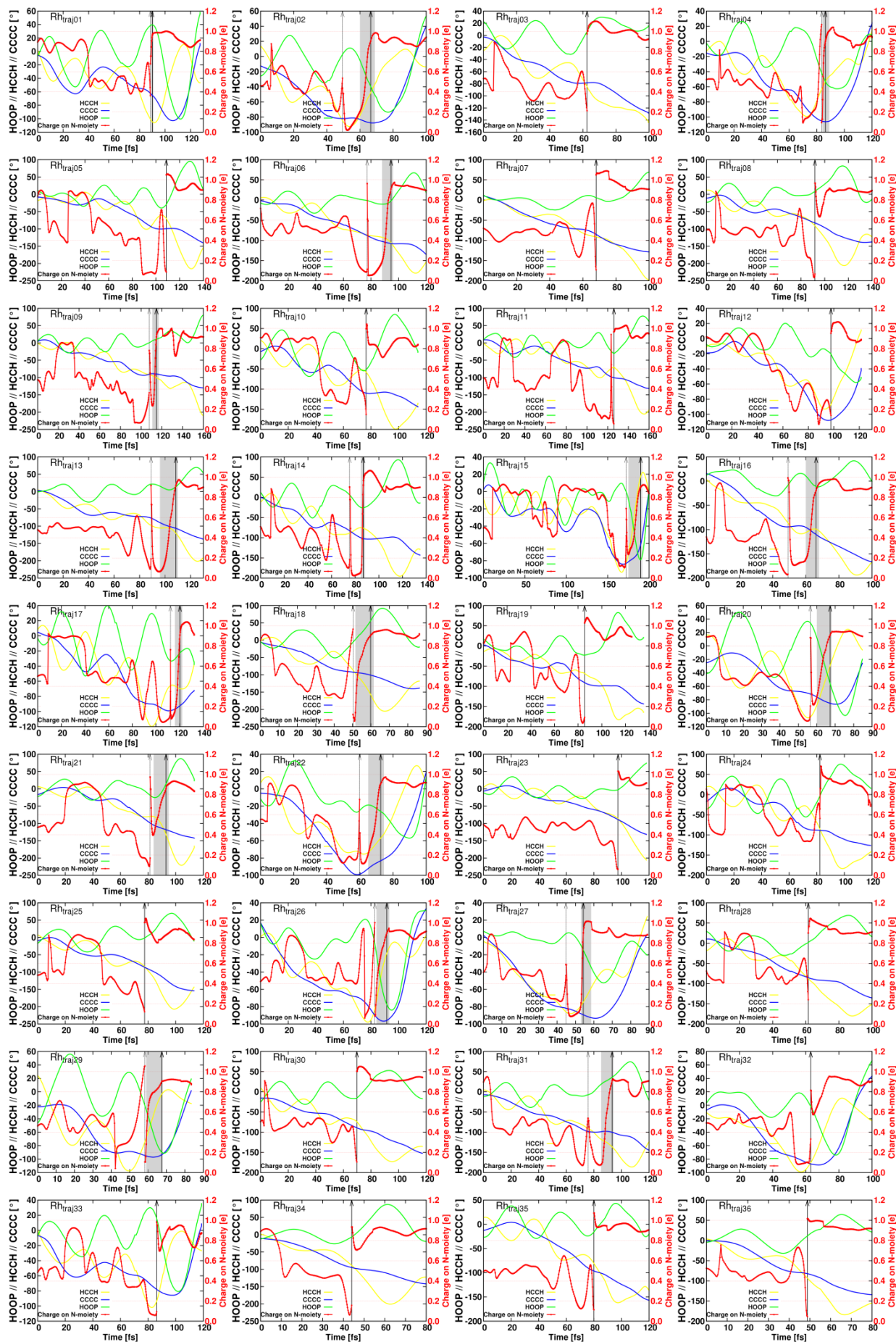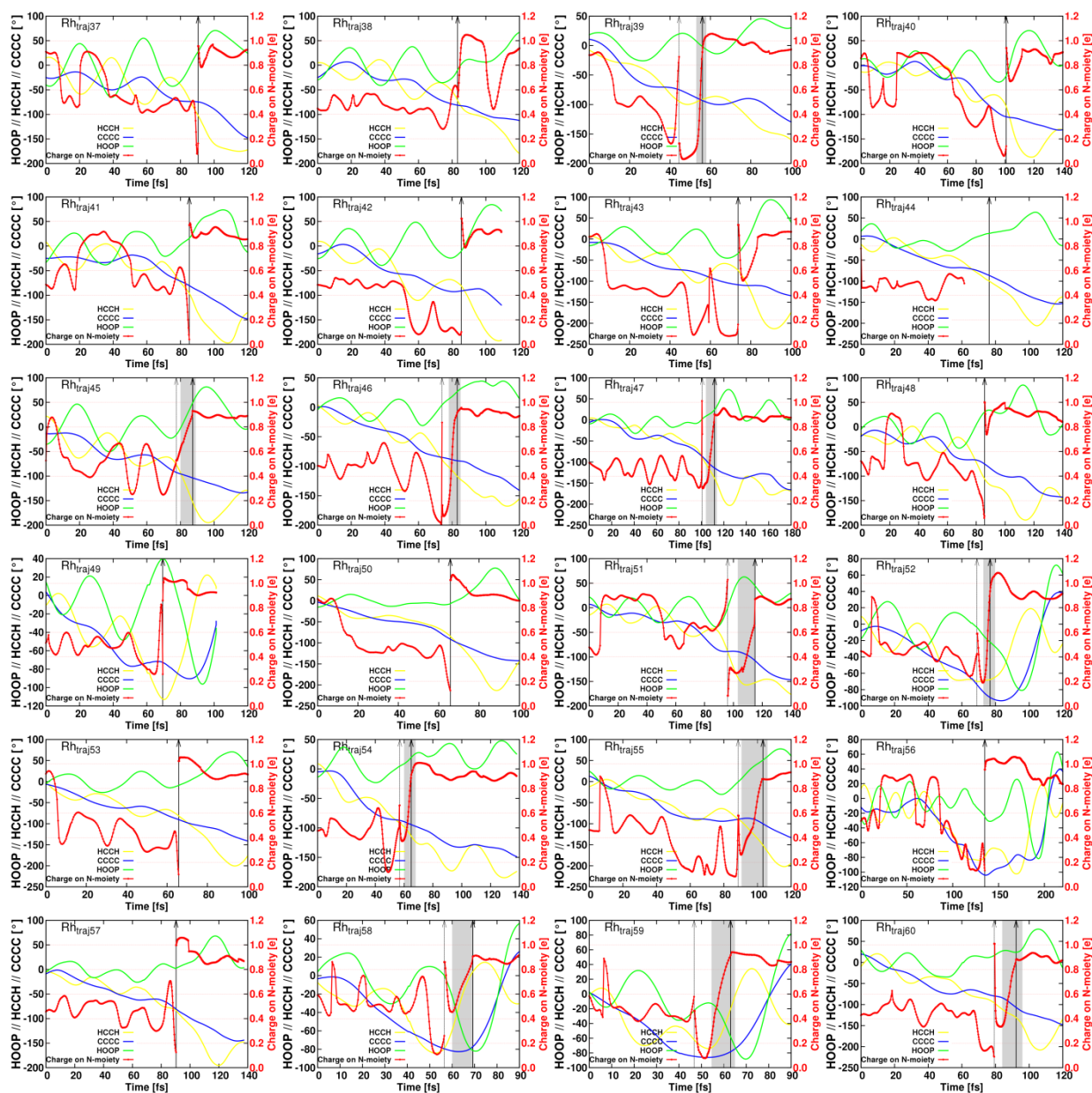
Figure S12. Evolution of $C_{10}C_{11}C_{12}C_{13}$, $H_{11}C_{11}C_{12}H_{12}$, HOOP and charge on N-moiety for each trajectory of Rh during the simulation time, gray-shaded areas denote the time span in which the WF changes from CT to covalent after a hopping event, vertical dashed and solid arrows show the hopping and decision times, respectively.
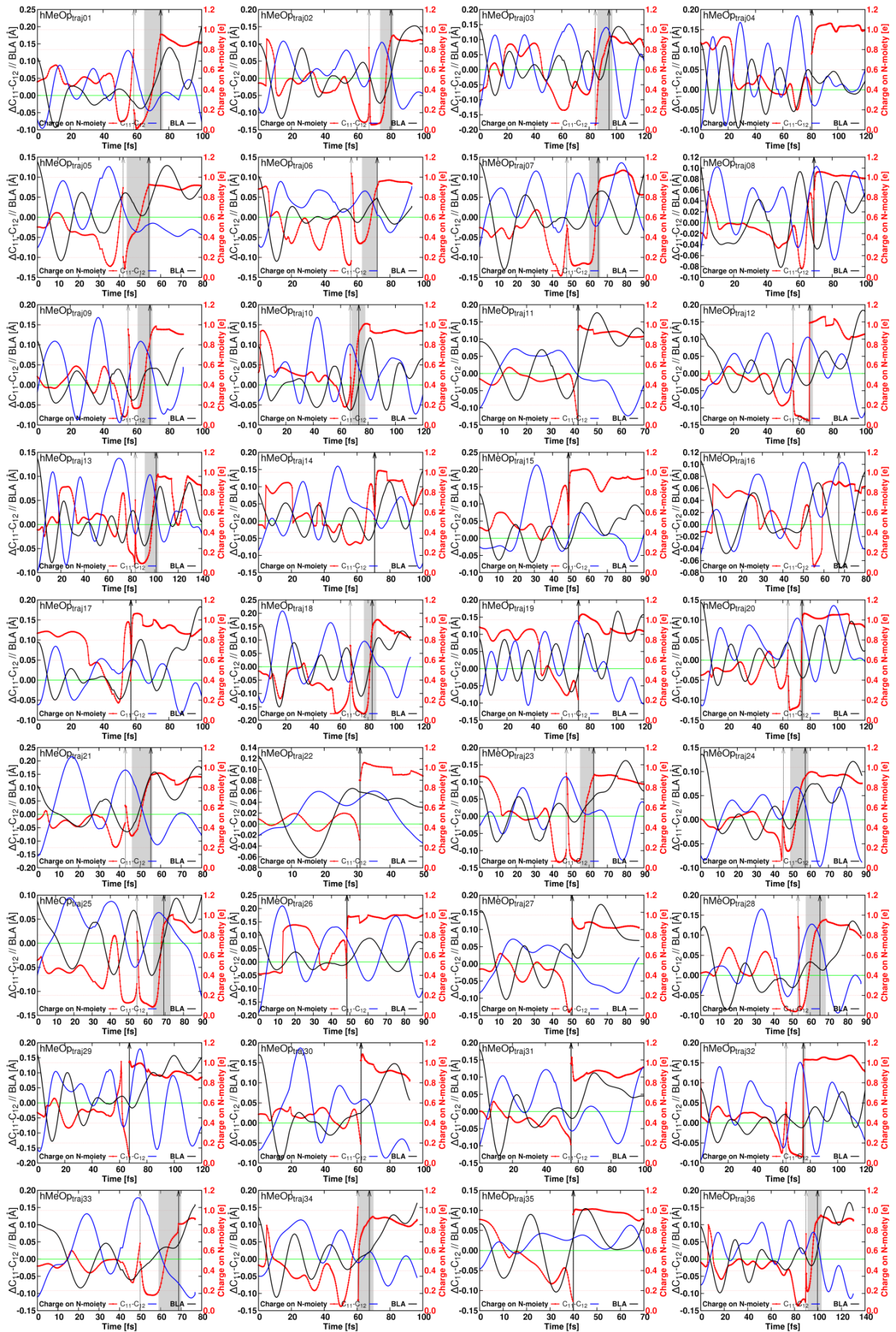
continue Figure S13
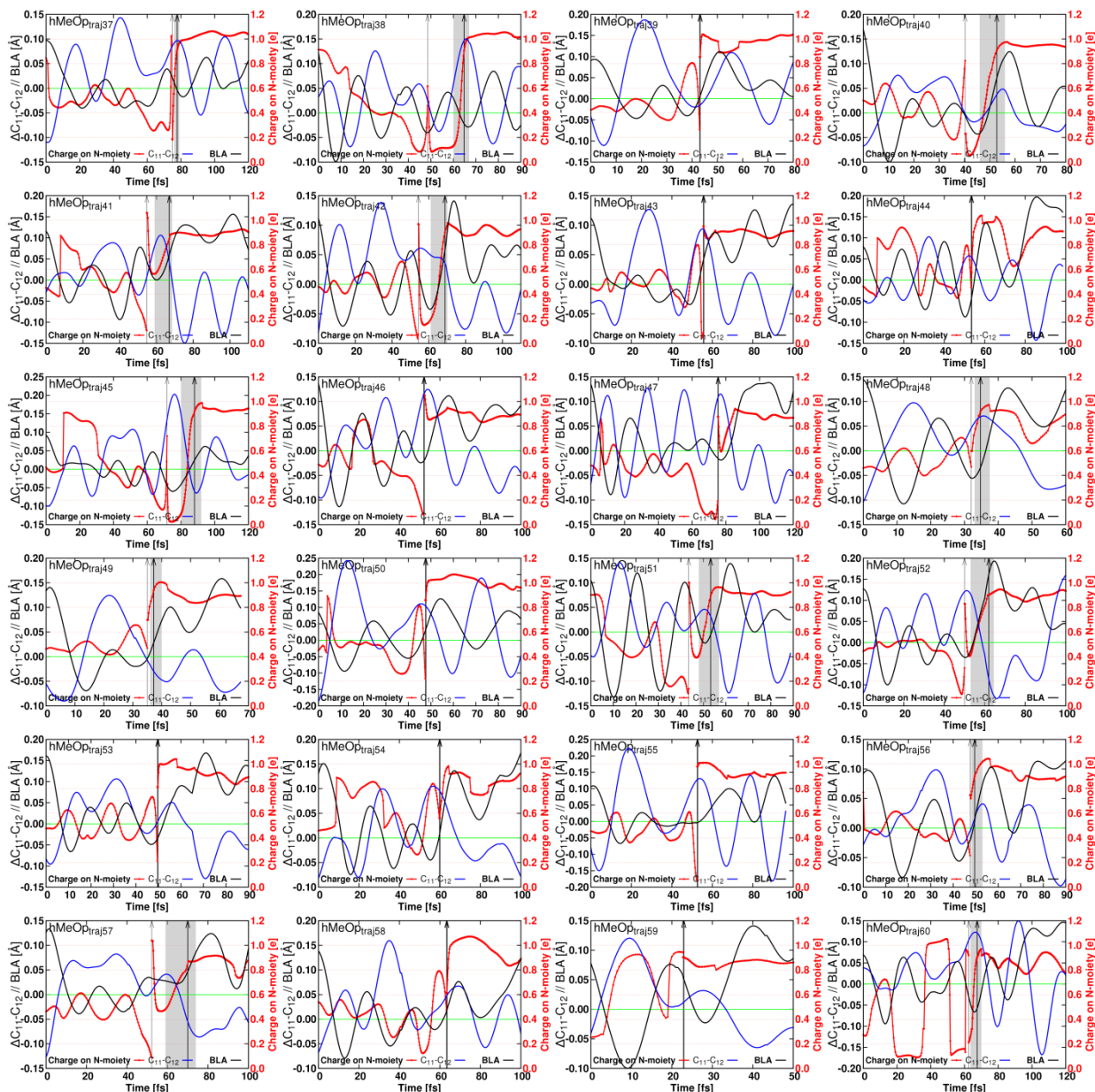
Figure S13. Evolution of BLA, $C_{11}C_{12}$ and charge on N-moiety for each trajectory of hMeOp during the simulation time (ΔC_{11}-C_{12} represents the deviation of C_{11}-C_{12} form 1.45Å), gray-shaded areas denote the time span in which the WF changes from CT to covalent after a hopping event, vertical dashed and solid arrows show the hopping and decision times, respectively.
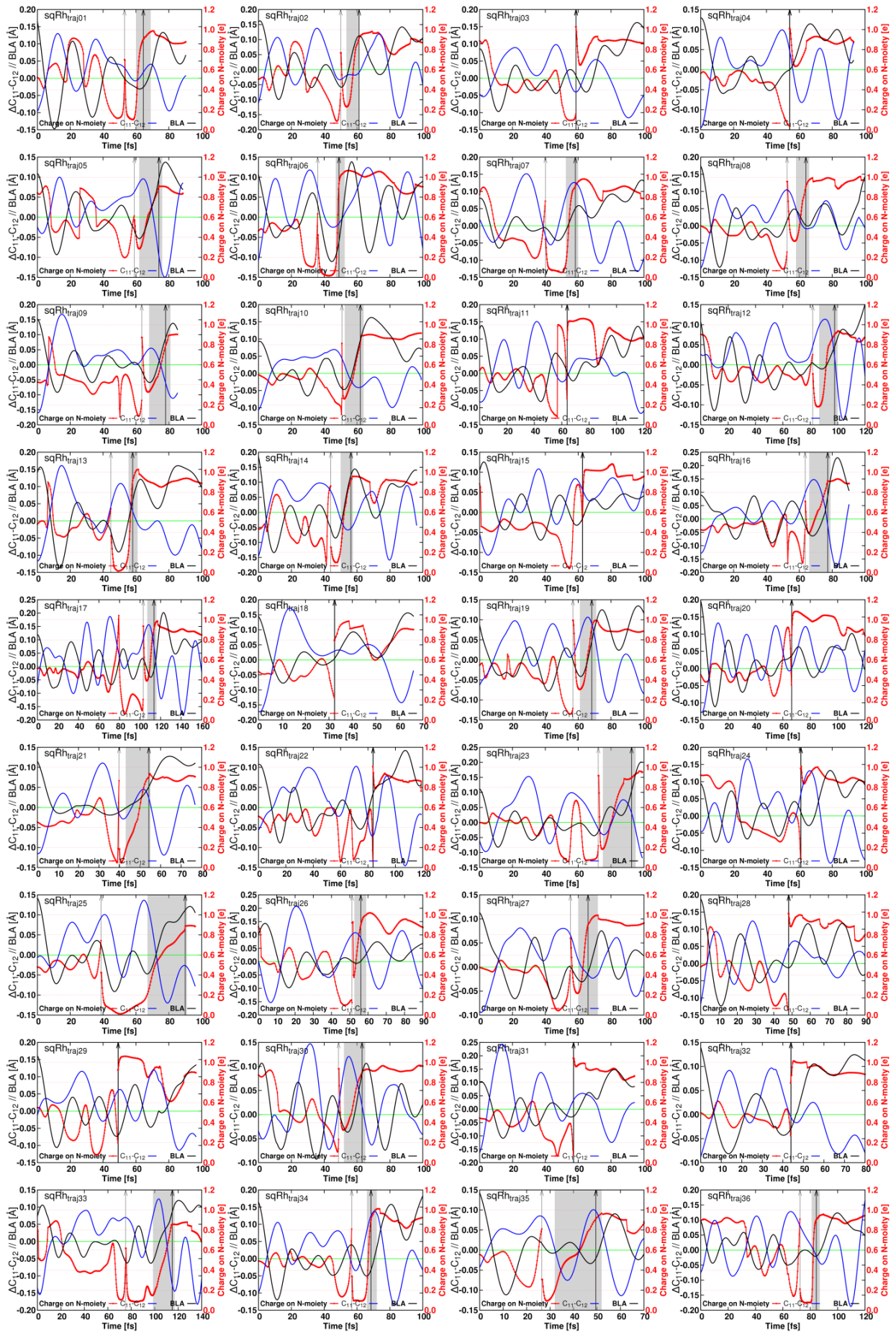
continue Figure S14
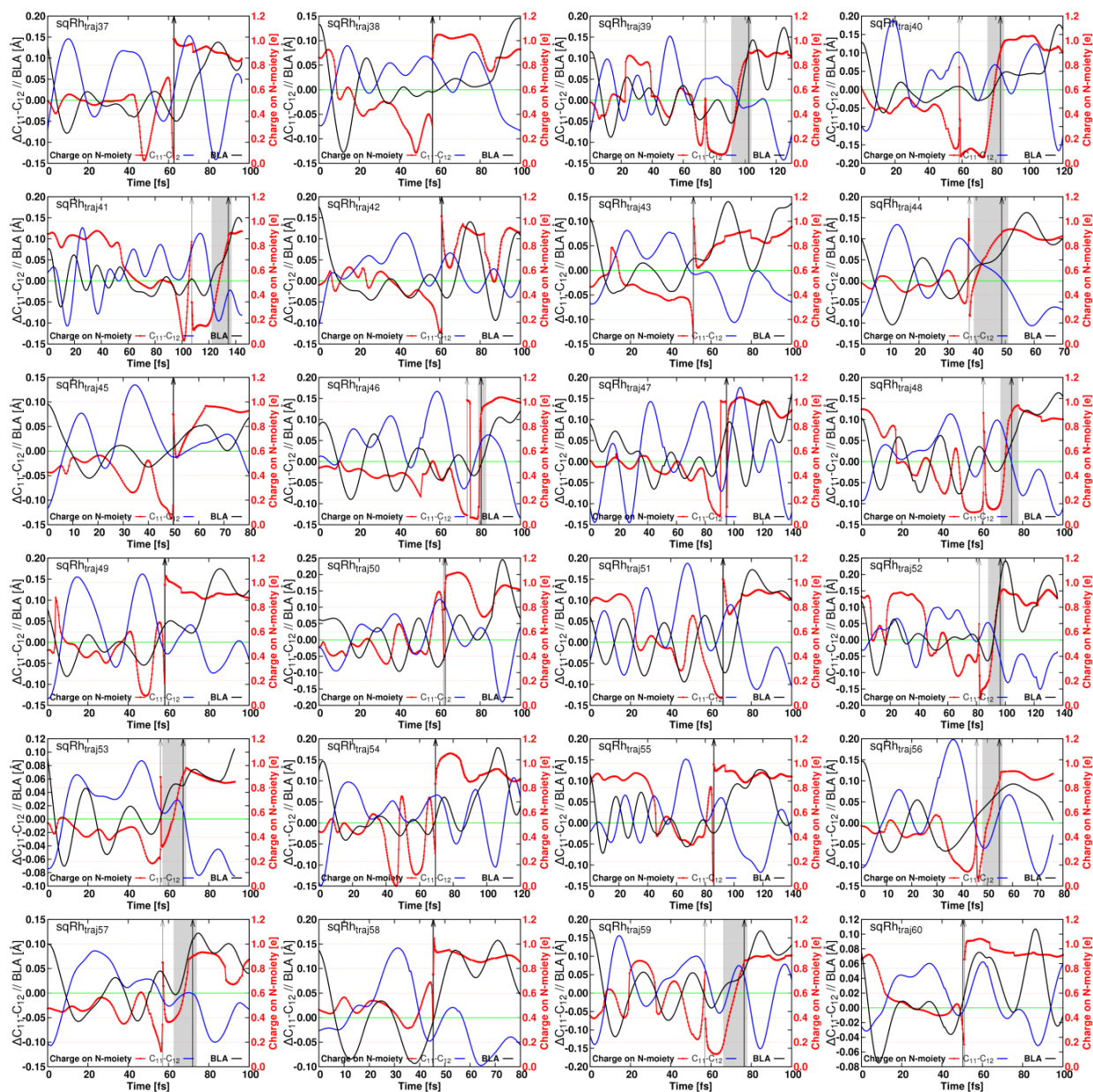
Figure S14. Evolution of BLA, $C_{11}C_{12}$ and charge on N-moiety for each trajectory of sqRh during the simulation time (ΔC_{11}-C_{12} represents the deviation of C_{11}-C_{12} form 1.45Å), gray-shaded areas denote the time span in which the WF changes from CT to covalent after a hopping event, vertical dashed and solid arrows show the hopping and decision times, respectively.
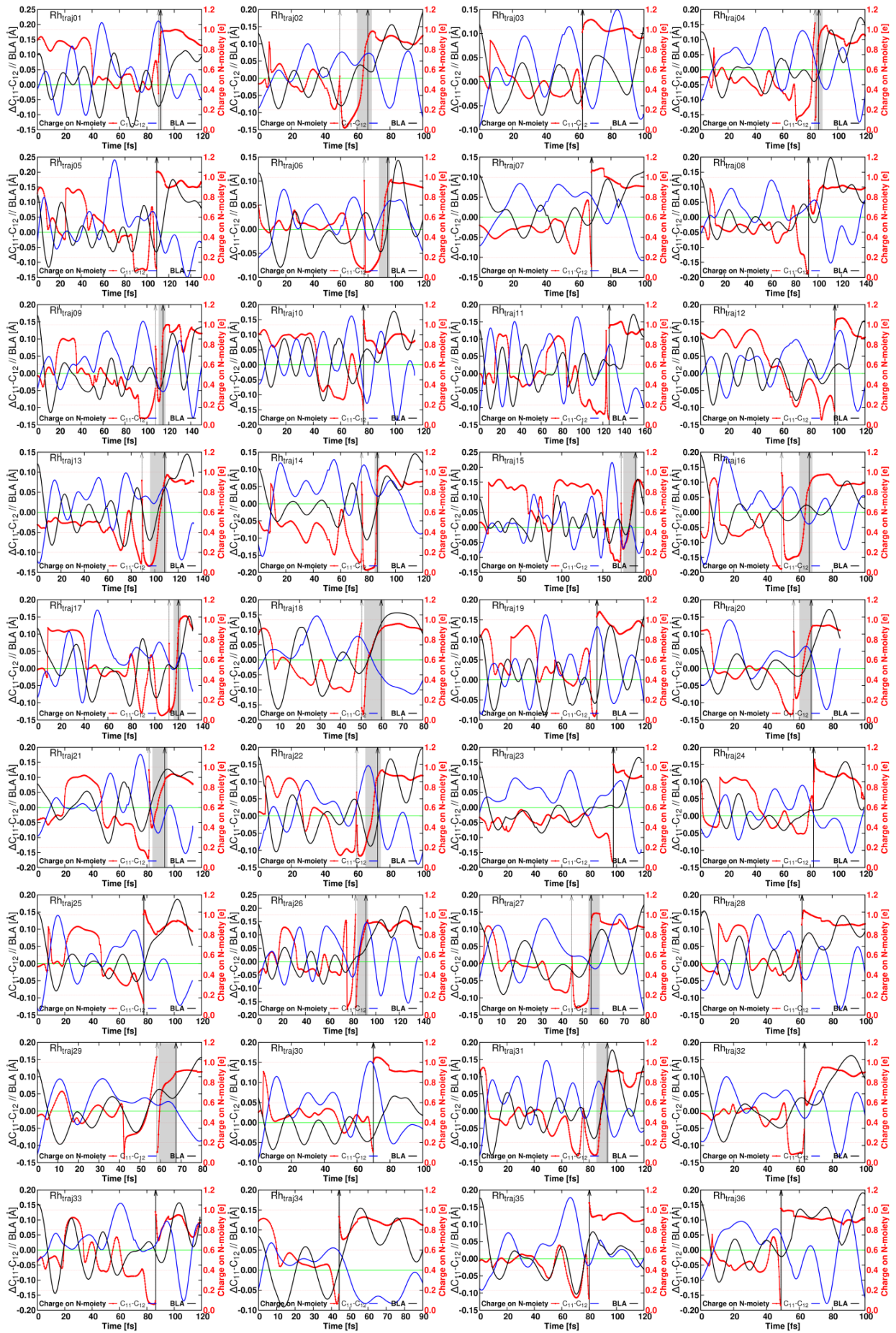
continue Figure S15
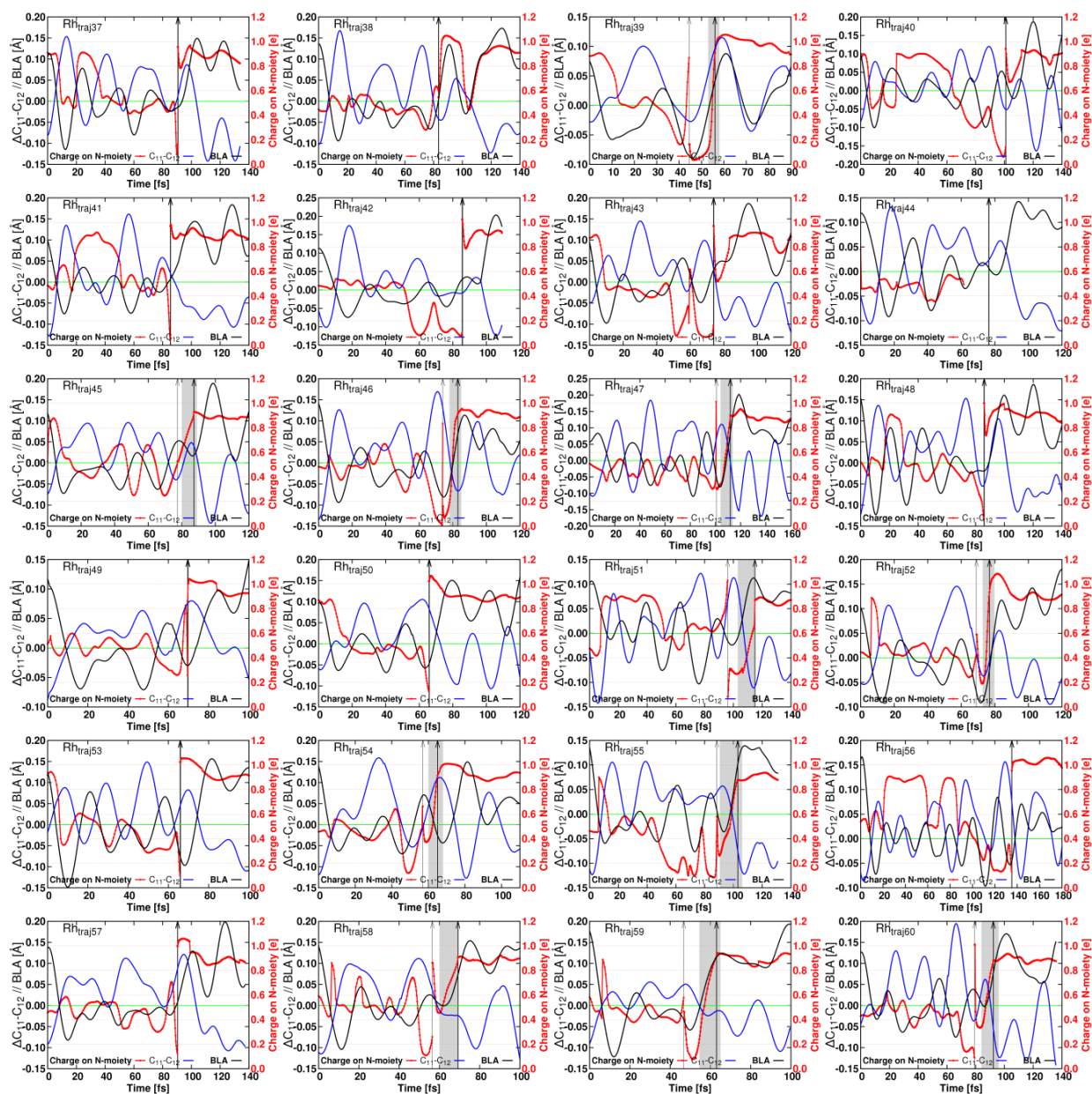
Figure S15. Evolution of BLA, $C_{11}C_{12}$ and charge on N-moiety for each trajectory of Rh during the simulation time (ΔC_{11}-C_{12} represents the deviation of C_{11}-C_{12} form 1.45Å), gray-shaded areas denote the time span in which the WF changes from CT to covalent after a hopping event, vertical dashed and solid arrows show the hopping and decision times, respectively.

Table S5. Classification the trajectories according to correlation between the BLA and the switching of the electronic structure toward covalent state.

|		Rh	sqRh	hMeOp
hop occurs with covalent characters (i.e. decision is taken at hop)	the WF adopts covalent character upon hop to the GS, thus, hop and decision time coincide; BLA is not decisive in these cases	3, 5, 7, 8, 10, 11, 12, 19, 23, 24, 25, 28, 30, 32, 33, 34, 35, 36, 37, 38, 40, 41, 42, 43, 44, 48, 49, 50, 53, 56, 57	3, 4, 11, 15, 18, 20, 22, 24, 28, 29, 31, 32, 37, 38, 42, 43, 47, 49, 50, 51, 54, 55, 58, 60	4, 8, 11, 14, 15, 16, 17, 19, 22, 26, 27, 29, 30, 31, 35, 39, 43, 44, 46, 47, 50, 53, 54, 55, 58, 59
	number of trajectries	**31**	**24**	**26**
the switching to biradical WF occurs after hopping time (i.e. at the decision time)	BLA increases and while C_{11}-C_{12} decreases when the GS WF character changes from CT to covalent	1, 4, 9, 14, 15, 18, 20, 21, 22, 27, 31, 46, 47, 51, 55, 58, 59, 60	5, 9, 10, 12, 13, 14, 16, 17, 19, 23, 26, 27, 30, 33, 39, 44, 48, 52	2, 3, 6, 7, 9, 10, 12, 13, 18, 21, 24, 25, 32, 33, 41, 42, 45, 49, 51, 52, 57, 60
	number of trajectries	**18**	**18**	**22**
	only BLA decreases when the GS WF character changes from CT to covalent	6, 13, 17, 26, 39, 52	1, 2, 6, 7, 21, 25, 34, 40, 41, 45, 46, 53, 56, 57, 59	1, 5, 23, 34, 36, 40, 48, 56
	number of trajectries	**6**	**15**	**8**
	BLA decreses when the GS WF character changes from CT to covalent	2, 16, 29, 45, 54	8, 35, 36	20, 28, 37, 38
	number of trajectries	**5**	**3**	**4**

7   Statistical Results

The distribution of S_1/S_0 energy gaps at the decay points shows that a non-negligible percentage of the ensemble decays while the S_1/S_0 gap is relatively large. However, most of the trajectories decay to the ground state close to the crossing, and the number of decay events decreases with the increase of the S_0/S_1 energy gap (**Figure S16**). **Figure S17** depicts the distribution of hopping events as a function of the CCCC torsion value, exhibiting a typical Gaussian like shape centered around 80-90°. The average retinal coordinates over all ensemble members at the decay points are given in **Table S6**, showing similar properties for all pigments.
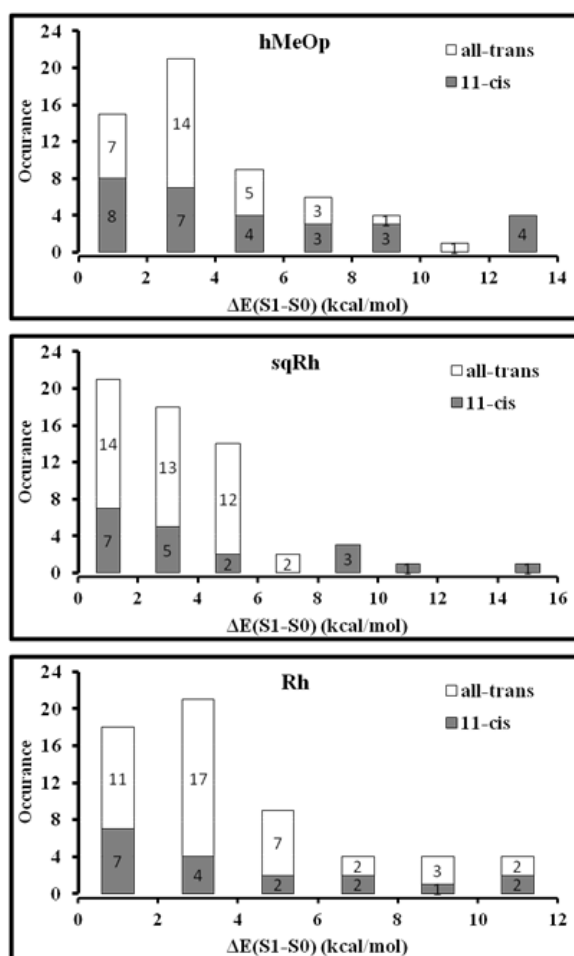
Figure S16. Distribution of hopping events as a function of the CASSCF energy differences $\Delta E(S_1-S_0)$ for hMeOp (top), sqRh (middle) and Rh (bottom). The height of the bar graphs corresponds to the number of trans (nofill) and cis (gray) photoproducts of individual trajectories.
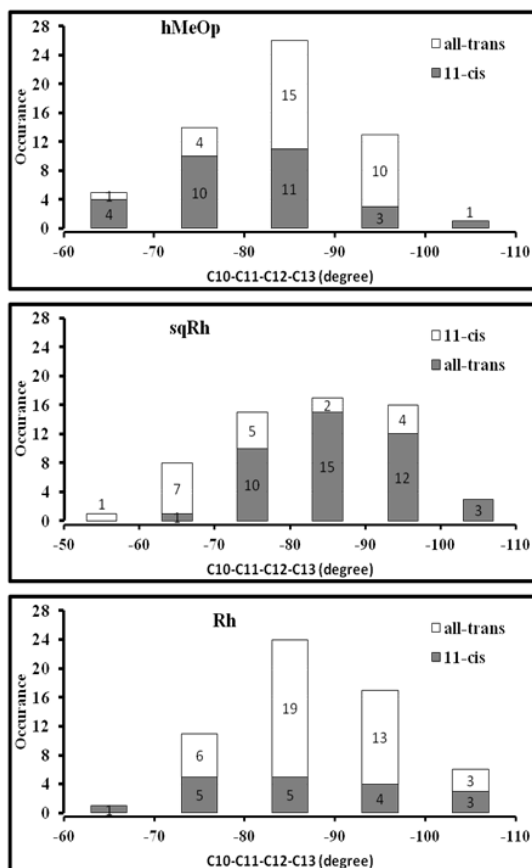
Figure S17. Distribution of hopping events as a function of the C_{10}–C_{11}–C_{12}–C_{13} torsion for hMeOp (top), sqRh (middle) and Rh (bottom). The height of the bar graphs corresponds to the number of trans (nofill) and cis (gray) photoproducts of individual trajectories.

Table S6. Averaged retinal geometry parameters in the three pigments at the hopping point.

Parameter	hMeOp	sqRh	Rh
C_5–C_6	1.339	1.333	1.345
C_6–C_7	1.482	1.478	1.489
C_7–C_8	1.380	1.375	1.373
C_8–C_9	1.445	1.436	1.427
C_9–C_{10}	1.421	1.438	1.450
C_{10}–C_{11}	1.388	1.382	1.381
C_{11}–C_{12}	1.492	1.481	1.482
C_{12}–C_{13}	1.373	1.378	1.370
C_{13}–C_{14}	1.453	1.468	1.466
C_{14}–C_{15}	1.369	1.369	1.366
C_{15}–N	1.375	1.384	1.365
C_8–C_9–C_{10}–C_{11}	143.3	143.3	149.1
C_{10}–C_{11}–C_{12}–C_{13}	84.0	83.4	88.1
C_{12}–C_{13}–C_{14}–C_{15}	167.7	165.4	166.3
C_8–C_9–C_{10}–H	23.7	25.2	24.3
H–C_{11}–C_{12}–C_{13}	90.1	89.7	87.6
C_{10}–C_{11}–C_{12}–H	97.6	96.6	99.6
C_{12}–C_{13}–C_{17}–H	15.4	15.7	14.7
H–C_{15}–N–H	165.5	165.4	167.1
H–C_{11}–C_{12}–H	88.3	90.2	84.8

Table S7*. Statistical analysis of the individual trajectories of the hMeOp ensemble showing the hopping /decision times, the direction of the $HC_{11}C_{12}H$, HOOP, $CC_{11}C_{12}C$ and the leading modes, and the computed and expected photoproduct distributions at both hopping/decision times.

Traj	hopping time (fs)	Product formation follows …			leading mode	decision time (fs)	Product formation follows …			leading mode	Computed Product		Expected Product at hopping time		Expected Product at decision time	
		HC_{11}-$C_{12}H$ at hopping time	HOOP at hopping time	$CC_{11}C_{12}C$ at hopping time			$HC_{11}C_{12}H$ at decision time	HOOP at decision time	$CC_{11}C_{12}C$ at decision time		Trans	Cis	Trans	Cis	Trans	Cis
01	58.75	T	T	F	HCCH	75.00	T	F	T	CCCC		√		√		√
02	67.25	T	T	F	HCCH	80.75	T	T	T	HCCH		√		√		√
03	84.50	T	T	T	HCCH	94.50	T	T	T	HCCH	√		√		√	
04	81.00	T	T	T	N/A	81.00	T	T	F	N/A		√		√		√
05	41.75	T	F	T	CCCC	54.25	T	T	T	HCCH	√		√		√	
06	56.50	T	T	T	HCCH	72.25	N/A	F	T	CCCC	√		√		-	
07	47.75	F	F	N/A	HCCH	65.00	F	T	N/A	N/A		√	√		√	
08	68.75	F	F	T	N/A	68.75	F	F	T	N/A	√			√		√
09	55.25	T	N/A	T	CCCC	68.50	T	N/A	T	HCCH	√		√		√	
10	67.00	T	N/A	T	CCCC	73.25	F	F	T	CCCC	√		√			√
11	41.75	T	T	T	HCCH/CCCC	41.75	T	T	T	HCCH	√		√		√	
12	57.00	F	F	N/A	N/A	66.25	T	F	T	CCCC		√	√			√
13	83.50	T	N/A	T	HCCH	101.25	T	T	F	HCCH	√		√		√	
14	70.50	F	F	T	CCCC	70.50	N/A	F	T	CCCC		√	√		-	
15	48.50	T	T	T	HCCH	48.50	T	T	T	HCCH	√		√		√	
16	67.00	F	F	T	CCCC	67.00	F	F	T	CCCC	√			√		√
17	56.75	T	T	F	HCCH	56.75	T	T	F	HCCH		√		√		√
18	67.00	T	T	F	CCCC	83.00	F	F	T	CCCC		√		√	√	
19	72.00	T	F	T	CCCC	72.00	T	F	T	CCCC	√		√		√	
20	63.75	F	N/A	F	CCCC	74.00	T	T	F	HCCH		√	√			√
21	42.75	T	T	F	HCCH	55.25	T	T	T	HCCH		√		√		√
22	30.75	T	T	T	HCCH	30.75	T	T	T	HCCH	√		√		√	
23	47.50	T	T	T	HCCH	62.50	T	T	T	HCCH		√		√		√
24	45.25	T	F	T	CCCC	57.25	T	T	T	HCCH	√		√		√	
25	54.50	T	T	T	HCCH	69.25	T	N/A	T	HCCH/CCCC		√		√		√
26	48.25	T	T	T	HCCH	48.25	T	T	T	HCCH	√		√		√	
27	50.50	T	T	T	HCCH	50.50	T	T	T	HCCH	√		√		√	
28	53.25	T	T	F	HCCH	65.25	T	T	N/A	HCCH		√		√		√
29	67.00	T	T	F	HCCH	67.00	T	T	F	HCCH		√		√		√
30	62.25	T	T	T	HCCH	62.25	T	T	T	HCCH	√		√		√	
31	55.50	T	T	N/A	HCCH	55.50	T	T	N/A	HCCH	√		√		√	
32	62.00	T	T	F	CCCC	75.00	F	F	T	N/A		√		√	√	
33	50.00	F	F	F	N/A	68.75	T	T	T	HCCH		√	√			√
34	60.50	T	T	T	HCCH	67.50	T	T	T	HCCH		√		√		√
35	39.75	T	N/A	T	HCCH/CCCC	39.75	T	N/A	T	HCCH/CCCC	√		√		√	
36	89.75	T	F	N/A	HCCH	99.50	T	T	T	HCCH		√		√		√

Continue Table S7

Traj	hopping time (fs)	HC_{11}-$C_{12}H$ at hopping time	HOOP at hopping time	$CC_{11}C_{12}C$ at hopping time	leading mode	decision time (fs)	$HC_{11}C_{12}H$ at decision time	HOOP at decision time	$CC_{11}C_{12}C$ at decision time	leading mode	Computed Product Trans	Computed Product Cis	Expected hopping Trans	Expected hopping Cis	Expected decision Trans	Expected decision Cis
		*Product formation follows …					Product formation follows …				Computed Product		Expected Product at hopping time		Expected Product at decision time	
37	74.75	F	T	F	N/A	77.75	T	T	F	N/A		√	√			√
38	48.50	T	F	T	N/A	64.75	F	F	T	N/A		√	√		√	
39	43.00	T	N/A	T	HCCH	43.00	T	T	T	N/A	√		√		√	
40	40.25	T	T	T	HCCH	52.75	T	T	T	HCCH	√		√		√	
41	54.75	T	T	T	HCCH	67.00	T	T	T	HCCH	√		√		√	
42	54.25	T	T	T	CCCC	68.75	T	T	T	HCCH	√		√		√	
43	55.50	T	T	N/A	HCCH	55.50	T	T	N/A	HCCH	√		√		√	
44	53.25	F	T	F	HCCH	53.25	F	T	F	HCCH		√	√		√	-
45	71.75	T	T	T	HCCH	88.00	T	T	T	HCCH	√		√		√	
46	52.00	T	T	T	HCCH	52.00	T	T	T	HCCH	√		√		√	
47	75.25	T	T	F	HCCH	75.25	T	T	F	HCCH		√		√		√
48	32.00	T	T	F	HCCH	34.75	T	T	F	HCCH		√		√		√
49	35.00	T	T	F	HCCH	37.25	T	T	F	HCCH		√		√		√
50	47.50	T	T	N/A	HCCH	47.50	T	T	N/A	HCCH	√		√		√	
51	43.50	T	T	T	HCCH	53.25	T	T	T	HCCH	√		√		√	
52	50.00	T	T	T	HCCH	62.00	T	T	T	HCCH	√		√		√	
53	49.50	T	T	N/A	HCCH	49.50	T	T	N/A	HCCH	√		√		√	
54	59.75	T	T	F	HCCH	59.75	T	T	F	HCCH		√		√		√
55	52.50	T	T	F	HCCH	52.50	T	T	F	HCCH	√		√		√	
56	47.50	N/A	T	F	CCCC	49.50	T	T	F	HCCH		√				√
57	52.25	T	F	T	HCCH	70.00	F	T	T	CCCC	√		√			√
58	63.25	T	T	N/A	HCCH	63.25	T	T	N/A	HCCH		√		√		√
59	22.75	T	T	F	HCCH	22.75	T	T	F	HCCH		√		√		√
60	62.50	T	T	N/A	N/A	67.50	F	F	T	N/A		√		√	√	
Average	56.9					63.7				Sum	31	29	36	23	31	26
Time shift from hopping to decision time = 6.8 fs										%	52	48	61	39	54	46

	leading mode			leading mode	
	HCCH (HOOP works)	39-41		HCCH	41-43
	CCCC	12-14		CCCC	9-11
	N/A	7		N/A	8
	HOOP breaks (or N/A)	18		HOOP breaks (or N/A)	12-15
	HCCH breaks (or N/A)	10		HCCH breaks (or N/A)	10-12

*where T refers to the trajectory in which the direction of the mode is in line with the computed photoproduct, F is opposite to T while N/A refers to the cases at which the direction is not clear or at turning point. The decision time is the time at which the WF is changed to a biradical one. The leading mode is the one which exhibits the largest deformation at the hopping/decision times, the average hopping time and τ (defined as the time period it takes for half of the population to decay to the GS) are roughly identical. The assignment in each trajectory is carried out using the specific figure for $HC_{11}C_{12}H$, HOOP, $CC_{11}C_{12}C$ and charges on N-moiety given in **Figure S10**.

Table S8*. Statistical analysis of the individual trajectories of the sqRh ensemble showing the hopping/decision times, the direction of the $HC_{11}C_{12}H$, HOOP, $CC_{11}C_{12}C$ and the leading modes, and the computed and expected photoproduct distributions at both hopping/decision times.

Traj	hopping time (fs)	Product formation follows ...			leading mode	decision time (fs)	Product formation follows ...			leading mode	Computed Product		Expected Product at hopping time		Expected Product at decision time	
		HC_{11}-$C_{12}H$ at hopping time	HOOP at hopping time	$CC_{11}C_{12}C$ at hopping time			$HC_{11}C_{12}H$ at decision time	HOOP at decision time	$CC_{11}C_{12}C$ at decision time		Trans	Cis	Trans	Cis	Trans	Cis
01	53.00	T	T	F	HCCH	64.50	T	T	F	HCCH		√		√		√
02	50.00	T	N/A	T	CCCC	61.25	T	T	T	HCCH/CCCC	√		√		√	
03	58.50	T	F	T	CCCC	58.50	T	F	T	CCCC	√		√		√	
04	54.00	T	T	T	HCCH	54.00	T	T	T	HCCH	√		√		√	
05	59.00	T	T	F	HCCH	74.00	T	T	N/A	HCCH		√		√		√
06	36.00	F	F	T	N/A	49.00	T	T	N/A	HCCH	√			√	√	
07	40.00	T	T	T	HCCH	58.25	T	T	N/A	HCCH	√		√		√	
08	52.50	T	T	T	HCCH	64.00	T	T	T	HCCH	√		√		√	
09	63.50	T	T	N/A	HCCH	78.00	T	F	T	CCCC		√		√		√
10	50.75	T	T	T	HCCH	62.00	T	T	T	HCCH	√		√		√	
11	63.75	F	F	T	N/A	63.75	F	F	T	N/A	√			√		√
12	81.75	T	T	F	HCCH	97.75	T	N/A	T	CCCC		√		√		√
13	44.75	F	F	N/A	N/A	58.00	T	T	N/A	HCCH		√	√			√
14	44.00	T	T	N/A	HCCH	56.25	T	T	N/A	HCCH	√		√		√	
15	62.50	F	F	T	N/A	62.50	F	F	T	N/A	√			√		√
16	63.50	T	T	N/A	HCCH	77.25	T	F	T	CCCC		√		√		√
17	103.00	T	T	F	HCCH	113.50	N/A	F	T	CCCC	√		√		-	
18	32.25	F	T	F	N/A	32.25	F	T	F	HCCH/CCCC		√	√		√	
19	56.75	N/A	F	T	CCCC	68.25	T	N/A	T	HCCH	√		-			√
20	66.25	F	F	T	N/A	66.25	F	F	T	N/A	√			√		√
21	39.75	T	T	F	HCCH	54.25	T	T	T	HCCH		√		√		√
22	83.50	T	T	N/A	HCCH	83.50	T	T	N/A	HCCH	√		√		√	
23	72.25	T	N/A	T	CCCC	92.50	T	T	T	HCCH		√		√		√
24	60.75	T	T	T	HCCH	60.75	T	T	T	HCCH	√		√		√	
25	38.75	T	F	T	CCCC	**90.00**	F	T	T	CCCC	√		√		√	
26	51.25	T	T	T	HCCH	56.00	T	T	T	HCCH	√		√		√	
27	55.25	F	F	T	CCCC	66.00	T	T	T	HCCH	√			√	√	
28	48.00	T	T	T	HCCH	48.00	T	T	T	HCCH	√		√		√	
29	49.00	F	F	N/A	N/A	49.00	F	F	N/A	N/A	√			√		√
30	48.75	T	T	T	HCCH	63.00	T	T	T	HCCH	√		√		√	
31	57.00	T	T	N/A	HCCH	57.00	T	T	N/A	HCCH		√	√			√
32	43.75	T	T	N/A	HCCH	43.75	T	T	N/A	HCCH	√		√		√	
33	75.25	F	F	N/A	N/A	115.00	T	T	T	HCCH	√			√	√	
34	56.75	F	T	F	HCCH	68.50	T	T	N/A	HCCH		√	√			√
35	26.50	F	F	T	CCCC	49.50	T	T	T	HCCH	√			√	√	
36	72.50	T	T	T	HCCH	84.50	T	T	T	HCCH	√		√		√	

Continue Table S8

Traj	hopping time (fs)	HC_{11}-$C_{12}H$ at hopping time	HOOP at hopping time	$CC_{11}C_{12}C$ at hopping time	leading mode	decision time (fs)	$HC_{11}C_{12}H$ at decision time	HOOP at decision time	$CC_{11}C_{12}C$ at decision time	leading mode	Computed Product Trans	Computed Product Cis	Expected Product at hopping time Trans	Expected Product at hopping time Cis	Expected Product at decision time Trans	Expected Product at decision time Cis
37	62.50	T	T	F	HCCH	62.50	T	T	F	HCCH		√		√		√
38	56.25	F	F	T	N/A	56.25	F	F	T	N/A	√			√		√
39	74.25	T	F	T	CCCC	102.25	T	T	T	HCCH	√		√		√	
40	58.25	T	T	F	N/A	82.75	F	F	T	N/A		√	√		√	
41	107.25	T	T	F	HCCH	134.50	T	T	T	HCCH/CCCC		√	√			√
42	60.75	T	F	T	CCCC	60.75	T	F	T	CCCC	√		√		√	
43	51.00	T	T	T	HCCH	51.00	T	T	T	HCCH	√		√		√	
44	37.50	T	T	T	HCCH	48.75	T	T	T	HCCH	√		√		√	
45	49.75	N/A	F	T	HCCH	49.75	T	T	T	HCCH	√		-		√	
46	73.50	T	T	N/A	HCCH	80.50	T	T	N/A	HCCH	√		√		√	
47	94.50	T	T	F	HCCH	94.50	T	T	F	HCCH		√	√			√
48	60.50	N/A	T	T	HCCH	74.50	T	T	T	HCCH	√		-		√	
49	58.00	T	T	F	HCCH	58.00	T	T	F	HCCH		√	√			√
50	62.50	T	T	T	HCCH	62.50	T	T	T	HCCH		√	√		√	
51	65.75	T	T	N/A	HCCH	65.75	T	T	N/A	HCCH	√		√		√	
52	81.75	T	T	T	HCCH	96.50	T	T	T	HCCH	√		√		√	
53	56.00	T	T	T	HCCH	67.25	T	T	T	HCCH	√		√		√	
54	69.25	F	F	T	N/A	69.25	F	F	T	N/A		√	√		√	
55	85.75	T	T	T	HCCH	85.75	T	T	T	HCCH	√		√		√	
56	45.75	T	T	T	HCCH	54.75	T	T	T	HCCH	√		√		√	
57	57.00	T	T	T	HCCH	72.00	T	T	T	CCCC	√		√		√	
58	45.25	T	T	T	HCCH	45.25	T	T	T	HCCH	√		√		√	
59	57.00	F	F	N/A	N/A	76.50	T	T	T	HCCH		√	√			√
60	50.00	T	T	T	HCCH	50.00	T	T	T	HCCH	√		√		√	
Average	**58.9**					**68.4**				**Sum**	**41**	**19**	**37**	**21**	**39**	**20**
Time shift from hopping to decision time = 9.5 fs										**%**	**68**	**32**	**64**	**36**	**66**	**34**

	leading mode				leading mode	
	HCCH (HOOP works)	39			HCCH (HOOP works)	42-45
	CCCC	9			CCCC	8-11
	N/A	12			N/A	7
	HOOP breaks (or N/A)	20			HOOP breaks (or N/A)	14
	HCCH breaks (or N/A)	17			HCCH breaks (or N/A)	10

*where T refers to the trajectory in which the direction of the mode is in line with the computed photoproduct, F is opposite to T while N/A refers to the cases at which the direction is not clear or at turning point. The decision time is the time at which the WF is changed to a biradical one. The leading mode is the one which exhibits the largest deformation at the hopping/decision times, the average hopping time and τ (defined as the time period it takes for half of the population to decay to the GS) are roughly identical. The assignment in each trajectory is carried out using the specific figure for $HC_{11}C_{12}H$, HOOP, $CC_{11}C_{12}C$ and charges on N-moiety given in **Figure S11**.

Table S9*. Statistical analysis of the individual trajectories of the Rh ensemble showing the hopping /decision times, the direction of the $HC_{11}C_{12}H$, HOOP, $CC_{11}C_{12}C$ and the leading modes, and the computed and expected photoproduct distributions at both hopping/decision times.

Traj	hopping time (fs)	HC_{11}-$C_{12}H$ at hopping time	HOOP at hopping time	$CC_{11}C_{12}C$ at hopping time	leading mode	decision time (fs)	$HC_{11}C_{12}H$ at decision time	HOOP at decision time	$CC_{11}C_{12}C$ at decision time	leading mode	Computed Product		Expected Product at hopping time		Expected Product at decision time	
											Trans	Cis	Trans	Cis	Trans	Cis
01	88.50	F	F	F	N/A	90.00	T	T	F	HCCH		√	√			√
02	49.50	F	F	N/A	N/A	66.50	T	T	N/A	HCCH		√	√			√
03	62.50	T	T	N/A	HCCH	62.50	T	T	N/A	HCCH	√		√		√	
04	83.50	T	T	N/A	HCCH	86.25	T	T	N/A	HCCH		√		√		√
05	108.75	T	T	N/A	HCCH	108.75	T	T	N/A	HCCH	√		√		√	
06	77.25	T	F	T	CCCC	94.50	T	T	N/A	HCCH	√		√		√	
07	68.00	T	F	T	CCCC	68.00	T	F	T	CCCC	√		√		√	
08	91.75	T	T	T	HCCH	91.75	T	T	T	HCCH	√		√		√	
09	107.75	T	T	F	HCCH	114.75	T	T	T	HCCH	√		√		√	
10	76.50	T	T	N/A	HCCH	76.50	T	T	N/A	HCCH	√		√		√	
11	126.00	T	T	T	HCCH	126.00	T	T	T	HCCH	√		√		√	
12	97.75	T	T	T	HCCH	97.75	T	T	T	HCCH		√		√		√
13	89.00	T	N/A	T	CCCC	108.50	T	T	T	HCCH	√		√		√	
14	75.25	F	F	T	CCCC	86.75	T	T	N/A	HCCH	√			√	√	
15	172.25	T	T	T	HCCH	189.75	T	N/A	T	HCCH		√		√		√
16	49.25	T	T	F	HCCH	66.00	T	N/A	T	HCCH	√		√		√	
17	112.25	N/A	N/A	T	CCCC	120.25	N/A	F	T	CCCC		√	-		-	
18	50.25	T	T	T	HCCH	59.75	T	T	T	HCCH	√		√		√	
19	85.50	T	T	T	HCCH	85.50	T	T	T	HCCH	√		√		√	
20	56.50	T	T	F	HCCH	67.25	T	T	F	HCCH		√		√		√
21	81.50	N/A	F	T	CCCC	93.00	T	T	T	HCCH	√		-		√	
22	59.75	F	F	N/A	N/A	72.50	T	T	T	HCCH		√	√			√
23	97.50	T	T	T	HCCH	97.50	T	T	T	HCCH	√		√		√	
24	82.25	T	T	N/A	HCCH	82.25	T	T	N/A	HCCH	√		√		√	
25	77.50	T	T	T	HCCH	77.50	T	T	T	HCCH	√		√		√	
26	82.75	T	T	F	HCCH	91.50	T	T	T	HCCH		√		√		√
27	44.75	F	F	F	N/A	54.25	T	T	F	HCCH		√	√			√
28	61.50	T	T	T	HCCH	61.50	T	T	T	HCCH	√		√		√	
29	58.25	T	T	F	HCCH	67.50	T	T	F	HCCH		√		√		√
30	69.75	T	T	T	HCCH	69.75	T	T	T	HCCH	√		√		√	
31	75.75	T	T	N/A	HCCH	93.25	T	T	N/A	HCCH	√		√		√	
32	63.00	T	T	F	HCCH	63.00	T	T	F	HCCH		√		√		√
33	86.25	T	T	F	HCCH	86.25	T	T	F	HCCH		√		√		√
34	44.00	T	T	T	HCCH	44.00	T	T	T	HCCH	√		√		√	
35	80.00	T	T	T	HCCH	80.00	T	T	T	HCCH	√		√		√	
36	48.75	T	T	T	HCCH	48.75	T	T	T	HCCH	√		√		√	

Continue Table S9

Traj	hopping time (fs)	HC$_{11}$-C$_{12}$H at hopping time	HOOP at hopping time	CC$_{11}$C$_{12}$C at hopping time	leading mode	decision time (fs)	HC$_{11}$C$_{12}$H at decision time	HOOP at decision time	CC$_{11}$C$_{12}$C at decision time	leading mode	Computed Product Trans	Computed Product Cis	Expected Product at hopping time Trans	Expected Product at hopping time Cis	Expected Product at decision time Trans	Expected Product at decision time Cis
37	90.50	T	T	N/A	HCCH	90.50	T	T	N/A	HCCH	√		√		√	
38	83.25	T	T	T	HCCH	83.25	T	T	T	HCCH	√		√		√	
39	44.50	T	T	T	N/A	56.00	T	T	T	HCCH	√		√		√	
40	100.75	T	T	T	HCCH	100.75	T	T	T	HCCH	√		√		√	
41	85.25	T	T	T	HCCH	85.25	T	T	T	HCCH	√		√		√	
42	85.50	T	T	F	HCCH	85.50	T	T	F	HCCH	√		√		√	
43	73.75	T	T	N/A	HCCH	73.75	T	T	N/A	HCCH	√		√		√	
44	76.25	T	T	T	HCCH	76.25	T	T	T	HCCH	√		√		√	
45	77.50	T	T	T	HCCH	87.25	T	T	T	HCCH	√		√		√	
46	74.00	T	T	T	HCCH	83.00	T	T	T	HCCH	√		√		√	
47	100.75	T	T	T	HCCH	111.75	T	T	T	HCCH	√		√		√	
48	85.75	T	N/A	T	HCCH/CCCC	85.75	T	N/A	T	HCCH/CCCC	√		√		√	
49	69.50	T	T	F	HCCH	69.50	T	T	F	HCCH		√		√		√
50	65.75	T	T	T	HCCH	65.75	T	T	T	HCCH	√		√		√	
51	96.00	T	T	N/A	HCCH	115.00	F	F	T	CCCC	√		√			√
52	69.00	T	F	F	N/A	76.75	T	T	F	HCCH		√		√		√
53	65.75	T	T	T	HCCH	65.75	T	T	T	HCCH	√		√		√	
54	57.00	T	T	T	HCCH	65.00	T	T	T	HCCH/CCCC	√		√		√	
55	88.50	T	T	F	HCCH	103.00	T	T	T	HCCH	√		√		√	
56	135.00	T	T	N/A	HCCH/N/A	135.00	T	T	N/A	HCCH/N/A		√		√		√
57	90.25	T	T	T	HCCH	90.25	T	T	T	HCCH	√		√		√	
58	56.50	T	T	F	HCCH	69.25	T	F	T	CCCC		√		√		√
59	46.75	F	F	N/A	N/A	63.00	T	T	T	HCCH		√	√			√
60	79.25	T	T	T	HCCH	92.25	T	T	T	HCCH	√		√		√	
Average	**79.0**					**84.7**				**Sum**	42	18	45	13	41	18
Time shift from hopping to decision time = 5.7 fs										**%**	70	30	78	22	69	31

		leading mode	HCCH (HOOP works)	45-47		leading mode	HCCH	53-56
			CCCC	7-7			CCCC	4-6
			N/A	7-8			N/A	0-1
			HOOP breaks (or N/A)	13			HOOP breaks (or N/A)	7
			HCCH breaks (or N/A)	8			HCCH breaks (or N/A)	2

*where T refers to the trajectory in which the direction of the mode is in line with the computed photoproduct, F is opposite to T while N/A refers to the cases at which the direction is not clear or at turning point. The decision time is the time at which the WF is changed to a biradical one. The leading mode is the one which exhibits the largest deformation at the hopping/decision times, the average hopping time and τ (defined as the time period it takes for half of the population to decay to the GS) are roughly identical. The assignment in each trajectory is carried out using the specific figure for HC$_{11}$C$_{12}$H, HOOP, CC$_{11}$C$_{12}$C and charges on N-moiety given in the **Figure S12**.

8   References:

1.   Murakami, M.; Kouyama, T., Crystal structure of squid rhodopsin. *Nature* **2008,** *453* (7193), 363-367.

2.   Rinaldi, S.; Melaccio, F.; Gozem, S.; Fanelli, F.; Olivucci, M., Comparison of the isomerization mechanisms of human melanopsin and invertebrate and vertebrate rhodopsins. *Proceedings of the National Academy of Sciences* **2014,** *111* (5), 1714-1719.

3.   Okada, T.; Sugihara, M.; Bondar, A.-N.; Elstner, M.; Entel, P.; Buss, V., The Retinal Conformation and its Environment in Rhodopsin in Light of a New 2.2 Å Crystal Structure†. *J. Mol. Biol.* **2004,** *342* (2), 571-583.

4.   Punwong, C.; Owens, J.; Martínez, T. J., Direct QM/MM Excited-State Dynamics of Retinal Protonated Schiff Base in Isolation and Methanol Solution. *The journal of physical chemistry. B* **2015,** *119* (3), 704-714.

5.   Sekharan, S.; Altun, A.; Morokuma, K., QM/MM Study of Dehydro and Dihydro β-Ionone Retinal Analogues in Squid and Bovine Rhodopsins: Implications for Vision in Salamander Rhodopsin. *Journal of the American Chemical Society* **2010,** *132* (45), 15856-15859.

6.   Senn, H. M.; Thiel, W., QM/MM methods for biomolecular systems. *Angewandte Chemie (International ed. in English)* **2009,** *48* (7), 1198-229.

7.   Lin, H.; Truhlar, D. G., QM/MM: what have we learned, where are we, and where do we go from here? *Theoretical Chemistry Accounts* **2007,** *117* (2), 185.

8.   Altoè, P.; Stenta, M.; Bottoni, A.; Garavelli, M., A tunable QM/MM approach to chemical reactivity, structure and physico-chemical properties prediction. *Theor. Chem. Acc.* **2007,** *118* (1), 219-240.

9.   Roos, B.; Taylor, P. R.; Siegbahn, P. E. M., A complete active space SCF method (CASSCF) using a density matrix formulated super-CI approach. *Chem. Phys.* **1980,** *48* (2), 157-173.

10.   Ferré, N.; Olivucci, M., Probing the Rhodopsin Cavity with Reduced Retinal Models at the CASPT2//CASSCF/AMBER Level of Theory. *J. Am. Chem. Soc.* **2003,** *125* (23), 6868-6869.

11.   Ferré, N.; Cembran, A.; Garavelli, M.; Olivucci, M., Complete-active-space self-consistent-field/Amber parameterization of the Lys296–retinal–Glu113 rhodopsin chromophore-counterion system. *Theor. Chem. Acc.* **2004,** *112* (4), 335-341.

12.   Andersson, K.; Malmqvist, P. A.; Roos, B. O.; Sadlej, A. J.; Wolinski, K., Second-order perturbation theory with a CASSCF reference function. *J. Phys. Chem.* **1990,** *94* (14), 5483-5488.

13.   Bonvicini, A.; Demoulin, B.; Altavilla, S. F.; Nenov, A.; El-Tahawy, M. M. T.; Segarra-Martí, J.; Giussani, A.; Batista, V. S.; Garavelli, M.; Rivalta, I., Ultraviolet vision: photophysical properties of the unprotonated retinyl Schiff base in the Siberian hamster cone pigment. *Theor. Chem. Acc.* **2016,** *135* (4), 1-10.

14.   El-Tahawy, M. M. T.; Nenov, A.; Garavelli, M., Photoelectrochromism in the Retinal Protonated Schiff Base Chromophore: Photoisomerization Speed and Selectivity under a Homogeneous Electric Field at Different Operational Regimes. *J. Chem. Theory Comput.* **2016,** *12* (9), 4460-4475.

15.   Forsberg, N.; Malmqvist, P.-Å., Multiconfiguration perturbation theory with imaginary level shift. *Chem. Phys. Lett.* **1997,** *274* (1-3), 196-204.

16.   Ghigo, G.; Roos, B. O.; Malmqvist, P.-Å., A modified definition of the zeroth-order Hamiltonian in multiconfigurational perturbation theory (CASPT2). *Chem. Phys. Lett.* **2004,** *396* (1-3), 142-149.

17.   Demoulin, B.; El-Tahawy, M. M. T.; Nenov, A.; Garavelli, M.; Le Bahers, T., Intramolecular photo-induced charge transfer in visual retinal chromophore mimics: electron density-based indices at the TD-DFT and post-HF levels. *Theor. Chem. Acc.* **2016,** *135* (4), 1-10.

18.   Cembran, A.; Gonzalez-Luque, R.; Altoe, P.; Merchan, M.; Bernardi, F.; Olivucci, M.; Garavelli, M., Structure, spectroscopy, and spectral tuning of the gas-phase retinal chromophore: the beta-ionone "handle" and alkyl group effect. *J. Phys. Chem. A* **2005,** *109* (29), 6597-605.

19.   Rivalta, I.; Nenov, A.; Weingart, O.; Cerullo, G.; Garavelli, M.; Mukamel, S., Modelling Time-Resolved Two-Dimensional Electronic Spectroscopy of the Primary Photoisomerization Event in Rhodopsin. *J. Phys. Chem. B* **2014,** *118* (28), 8396-8405.

20.   Polli, D.; Altoe, P.; Weingart, O.; Spillane, K. M.; Manzoni, C.; Brida, D.; Tomasello, G.; Orlandi, G.; Kukura, P.; Mathies, R. A.; Garavelli, M.; Cerullo, G., Conical intersection dynamics of the primary photoisomerization event in vision. *Nature* **2010,** *467* (7314), 440-443.

21.   Frutos, L. M.; Andruniow, T.; Santoro, F.; Ferre, N.; Olivucci, M., Tracking the excited-state time evolution of the visual pigment with multiconfigurational quantum chemistry. *Proc. Natl. Acad. Sci. U. S. A.* **2007,** *104* (19), 7764-9.

22.   Sloane, C. S.; Hase, W. L., On the dynamics of state selected unimolecular reactions: Chloroacetylene dissociation and predissociation. *The Journal of Chemical Physics* **1977,** *66* (4), 1523-1533.

23.   Swope, W. C.; Andersen, H. C.; Berens, P. H.; Wilson, K. R., A computer simulation method for the calculation of equilibrium constants for the formation of physical clusters of molecules: Application to small water clusters. *J. Chem. Phys.* **1982,** *76* (1), 637-649.

24.   Granucci, G.; Persico, M., Critical appraisal of the fewest switches algorithm for surface hopping. *J. Chem. Phys.* **2007,** *126* (13), 134114.

25.   Werner, H.-J.; Knowles, P.; Lindh, R.; Manby, F. R.; Schütz, M.; Celani, P.; Korona, T.; Rauhut, G.; Amos, R.; Bernhardsson, A., MOLPRO, version 2010.1, a package of ab initio programs. *See* http://www/. molpro. net **2010**.

26.   Aquilante, F.; De Vico, L.; Ferré, N.; Ghigo, G.; Malmqvist, P.-å.; Neogrády, P.; Pedersen, T. B.; Pitoňák, M.; Reiher, M.; Roos, B. O.; Serrano-Andrés, L.; Urban, M.; Veryazov, V.; Lindh, R., MOLCAS 7: The Next Generation. *J. Comput. Chem.* **2009,** *31* (1), 224-247.

27.   Aquilante, F.; Autschbach, J.; Carlson, R. K.; Chibotaru, L. F.; Delcey, M. G.; De Vico, L.; Fdez. Galván, I.; Ferré, N.; Frutos, L. M.; Gagliardi, L.; Garavelli, M.; Giussani, A.; Hoyer, C. E.; Li Manni, G.; Lischka, H.; Ma, D.; Malmqvist, P. Å.; Müller, T.; Nenov, A.; Olivucci, M.; Pedersen, T. B.; Peng, D.; Plasser, F.; Pritchard, B.; Reiher, M.; Rivalta, I.; Schapiro, I.; Segarra-Martí, J.; Stenrup, M.; Truhlar, D. G.; Ungur, L.; Valentini, A.; Vancoillie, S.; Veryazov, V.; Vysotskiy, V. P.; Weingart, O.; Zapata, F.; Lindh, R., Molcas 8: New capabilities for multiconfigurational quantum chemical calculations across the periodic table. *J. Comput. Chem.* **2016,** *37* (5), 506-541.

28.   Garavelli, M.; Celani, P.; Bernardi, F.; Robb, M. A.; Olivucci, M., The C5H6NH2+ Protonated Shiff Base: An ab Initio Minimal Model for Retinal Photoisomerization. *Journal of the American Chemical Society* **1997,** *119* (29), 6891-6901.

29.   Matsuyama, T.; Yamashita, T.; Imamoto, Y.; Shichida, Y., Photochemical properties of mammalian melanopsin. *Biochemistry* **2012,** *51* (27), 5454-62.

30.   Suzuki, T.; Uji, K.; Kito, Y., Studies on cephalopod rhodopsin: photoisomerization of the chromophore. *Biochimica et biophysica acta* **1976,** *428* (2), 321-38.

31.   Hurley, J. B.; Ebrey, T. G.; Honig, B.; Ottolenghi, M., Temperature and wavelength effects on the photochemistry of rhodopsin, isorhodopsin, bacteriorhodopsin and their photoproducts. *Nature* **1977,** *270*, 540.

32.   Tomasello, G.; Olaso-González, G.; Altoè, P.; Stenta, M.; Serrano-Andrés, L.; Merchán, M.; Orlandi, G.; Bottoni, A.; Garavelli, M., Electrostatic Control of the Photoisomerization Efficiency and Optical Properties in Visual Pigments: On the Role of Counterion Quenching. *Journal of the American Chemical Society* **2009,** *131* (14), 5172-5186.

33.   Cembran, A.; Bernardi, F.; Olivucci, M.; Garavelli, M., The retinal chromophore/chloride ion pair: Structure of the photoisomerization path and interplay of charge transfer and covalent states. *Proceedings of the National Academy of Sciences of the United States of America* **2005,** *102* (18), 6255-6260.

34.   Gozem, S.; Luk, H. L.; Schapiro, I.; Olivucci, M., Theory and Simulation of the Ultrafast Double-Bond Isomerization of Biological Chromophores. *Chemical Reviews* **2017**.

35.   Hurley, J. B.; Ebrey, T. G.; Honig, B.; Ottolenghi, M., Temperature and wavelength effects on the photochemistry of rhodopsin, isorhodopsin, bacteriorhodopsin and their photoproducts. *Nature* **1977,** *270* (5637), 540-542.